



## Article

**Cite this article:** Hoffmann-Abdi K, Meyer H, Fernandoy F, Freitag J, Shaw FM, Werner M, Thomas ER, McConnell JR, Schneider C (2023). Deciphering stable water isotope records of firn cores from a strongly maritime, high-accumulation site on the Antarctic Peninsula. *Journal of Glaciology* 69(278), 2027–2045. <https://doi.org/10.1017/jog.2023.79>

Received: 15 November 2022

Revised: 28 August 2023

Accepted: 4 September 2023

First published online: 8 November 2023

**Keywords:**


accumulation; Antarctic glaciology; ice/atmosphere interactions; polar firn; snow and ice chemistry

**Corresponding author:**

Kirstin Hoffmann-Abdi;

Email: [Kirstin.Hoffmann@awi.de](mailto:Kirstin.Hoffmann@awi.de)

# Deciphering stable water isotope records of firn cores from a strongly maritime, high-accumulation site on the Antarctic Peninsula

Kirstin Hoffmann-Abdi<sup>1,2</sup> , Hanno Meyer<sup>1</sup>, Francisco Fernandoy<sup>3</sup>, Johannes Freitag<sup>4</sup>, Fyntan M. Shaw<sup>1</sup>, Martin Werner<sup>4</sup>, Elizabeth R. Thomas<sup>5</sup> , Joseph R. McConnell<sup>6</sup> and Christoph Schneider<sup>2</sup> 

<sup>1</sup>Alfred Wegener Institute, Helmholtz Centre for Polar and Marine Research, Research Unit Potsdam, Potsdam 14473, Germany; <sup>2</sup>Geography Department, Humboldt-Universität zu Berlin, Unter den Linden 6, Berlin 10099, Germany; <sup>3</sup>Facultad de Ingeniería, Universidad Nacional Andrés Bello, Viña del Mar 2531015, Chile; <sup>4</sup>Alfred Wegener Institute, Helmholtz Centre for Polar and Marine Research, Bremerhaven 27568, Germany; <sup>5</sup>Ice Dynamics and Paleoclimate, British Antarctic Survey, Cambridge CB3 0ET, UK and <sup>6</sup>Division of Hydrologic Sciences, Desert Research Institute, Reno, NV 89512, USA

**Abstract**

Stable water isotope records of six firn cores retrieved from two adjacent plateaus on the northern Antarctic Peninsula between 2014 and 2016 are presented and investigated for their connections with firn-core glacio-chemical data, meteorological records and modelling results. Average annual accumulation rates of  $2500 \text{ kg m}^{-2} \text{ a}^{-1}$  largely reduce the modification of isotopic signals in the snowpack by post-depositional processes, allowing excellent signal preservation in space and time. Comparison of firn-core and ECHAM6-wiso modelled  $\delta^{18}\text{O}$  and d-excess records reveals a large agreement on annual and sub-annual scales, suggesting firn-core stable water isotopes to be representative of specific synoptic situations. The six firn cores exhibit highly similar isotopic patterns in the overlapping period (2013), which seem to be related to temporal changes in moisture sources rather than local near-surface air temperatures. Backward trajectories calculated with the HYSPLIT model suggest that prominent  $\delta^{18}\text{O}$  minima in 2013 associated with elevated sea salt concentrations are related to long-range moisture transport dominated by westerly winds during positive SAM phases. In contrast, a broad  $\delta^{18}\text{O}$  maximum in the same year accompanied by increased concentrations of black carbon and mineral dust corresponds to the advection of more locally derived moisture with northerly flow components (South America) when the SAM is negative.

**1. Introduction**

The northern Antarctic Peninsula (AP) is a highly promising, but challenging site for paleoclimate studies. On the one hand, high accumulation rates ( $>2000 \text{ kg m}^{-2} \text{ a}^{-1}$ ) allow the preservation of usually rapidly dissipating chemical species in the snowpack (e.g. halogens, hydrogen peroxide), with temporal and spatial variations in concentration serving as indicators of climate and environmental changes (Fernandoy and others, 2012; Thomas and Tetzner, 2019). On the other hand, the strongly maritime character of the northern AP climate reduces or even blurs the seasonal cyclicity of stable water isotopes measured in firn and ice cores (Hoffmann-Abdi and others, 2021a). Therefore, the well-established interpretation of stable oxygen and hydrogen isotopes as proxies for the condensation temperature at the precipitation site (Dansgaard, 1964) has limited applicability to the northern AP. Instead, factors such as sea-ice variability and the formation of inversion layers during periods of sea-ice coverage need to be considered (Fernandoy and others, 2018).

The orographic characteristics of the AP create differences, e.g. in air temperature, precipitation and accumulation rates on relatively small spatial scales. The up to 2000 m high mountain chain that stretches along the AP acts as a barrier for precipitating air masses generally reaching the AP from the west, dividing it into a warmer and moister western side and a colder and drier eastern side (Vaughan and others, 2003; Carrasco and others, 2021). While the western side receives small to moderate amounts of precipitation on a high percentage of days per year, on the eastern side occasional extreme precipitation events due to incursions of moist air from the north play an important role in the annual snow accumulation (Turner and others, 2019). Accumulation rates show a strong west–east gradient across the AP, decreasing from  $\sim 3000 \text{ kg m}^{-2} \text{ a}^{-1}$  on the western side to  $\sim 500 \text{ kg m}^{-2} \text{ a}^{-1}$  on the eastern side (Thomas and Tetzner, 2019). Recent studies have highlighted the importance of atmospheric rivers for the AP region which can induce extremely high temperatures and deliver large amounts of precipitation (Maclennan and others, 2022), leading to intense surface melt events (Wille and others, 2019) and the destabilization of ice shelves (Wille and others, 2022).

The temporal variability of the westerly circumpolar vortex extending from the surface to the stratosphere dominates both, short- and long-term changes in atmospheric circulation of the Southern Hemisphere mid-high latitudes (Thompson and Wallace, 2000; Thompson and Solomon, 2002; Perren and others, 2020). The zonal strength and position of the belt of



tropospheric westerlies is determined by the phase of the Southern Annular Mode (SAM) which is the primary mode of atmospheric circulation variability at high southern latitudes (Limpasuvan and Hartmann, 2000; Thompson and Wallace, 2000; Marshall, 2003; Lee and others, 2019). When the SAM is in its positive phase, the circumpolar westerlies are strengthened and shifted poleward as the polar vortex contracts. Furthermore, the flow is more zonal, reducing the meridional heat and moisture exchange (Limpasuvan and Hartmann, 2000; Thompson and Wallace, 2000; Thompson and Solomon, 2002). Concurrently, the Amundsen Sea Low (ASL) deepens and is shifted to the south as well as to the east (Bellingshausen Sea sector), resulting in a stronger northwesterly flow across the AP (Fogt and others, 2012; Hosking and others, 2013; Raphael and others, 2016). The ASL is a climatological low-pressure centre located in the area of the Bellingshausen-Amundsen and Ross Seas between 60°–80°S and 170°E–62°W (Turner and others, 2013; Hosking and others, 2016). Its strength and particularly its longitudinal position influence the variability of the meridional wind field over this sector (Hosking and others, 2013). The axis of the westerly wind belt is usually located south of the northernmost end of the AP during positive SAM phases. Therefore, the AP experiences less advection of cold and dry air masses from the south in such periods (Thompson and Solomon, 2002). Contemporaneously, the transport of warm and moist air masses from more northerly latitudes of the Southern Ocean towards the western coast of the AP is facilitated, leading to increased precipitation and warmer than average conditions (Thompson and Solomon, 2002; Orr and others, 2004; Marshall and Thompson, 2016; Marshall and others, 2017). However, the steep orography of the AP forms a precipitation shadow on the eastern side, causing precipitation to decrease when the SAM is positive (Marshall and others, 2017). During a negative SAM phase, opposite anomalies of the circumpolar westerlies and the ASL prevail. Specifically for the AP, the then stronger meandering and thus more meridional westerly flow can cause either warm-air advection from the north, e.g. from the South Pacific Ocean, or cold-air advection from the south, i.e. from the Antarctic interior. The concurrent weakening of the circumpolar westerlies also favours the transport of more local moisture towards the northern AP (Schmidt and others, 2007) as well as air-mass advection from the Weddell Sea in the East.

Here we examine six firn cores drilled on the northern AP in three consecutive years, from 2014 to 2016, for common signals in their stable water isotope composition. We include firn cores from Plateau Laclavere (LCL; 63°27'S, 57°45'W, ~1100 m above sea level [a.s.l.]) and Plateau Louis Philippe (LP; 63°37'S, 58°27'W, ~1400–1500 m a.s.l.). Both plateaus are located at the ice divide of the northern AP that receives moisture primarily from the Bellingshausen-Amundsen Sea, but also from the South Pacific Ocean, the South American continent and occasionally the Weddell Sea (Fernandoy and others, 2012, 2018). LCL has been investigated by a Chilean-German research team since 2008 (Fernandoy and others, 2012, 2018; Hoffmann-Abdi and others, 2021a), while LP was explored for the first time in 2016. LCL is a 3 km wide and 6 km long, flat ice cap with annual accumulation rates of more than 2000 kg m<sup>-2</sup> a<sup>-1</sup> located ~19 km south-east of the Chilean station Bernardo O'Higgins (OH; 12 m a.s.l.; Fig. 1). LP is located ~40 km south of LCL (Fig. 1).

Previous studies have shown that stable water isotopes in snow and firn from LCL are not related to local near-surface air temperatures due to the strongly maritime climate of the northern AP, local post-depositional processes and the influence of sea-ice conditions (Fernandoy and others, 2012, 2018; Hoffmann-Abdi and others, 2021a). A correlation between  $\delta^{18}\text{O}$  of precipitation and near-surface air temperatures was only found for OH station

for the period 2008–2014. This correlation varies considerably depending on the season (Fernandoy and others, 2018).

This paper aims to improve the interpretation of subannual stable water isotope records obtained from snow and firn on the northern AP, and to define their relationship to meso- and large-scale atmospheric circulation patterns. For this purpose, we (1) intercompare the stable water isotope composition of different firn cores to determine whether common patterns can be identified in the records, (2) investigate the spatial and temporal variability in the isotopic records through model-data-intercomparisons, (3) assess signal preservation and post-depositional processes and (4) test how the isotopic signals relate to intra-annual synoptic and atmospheric circulation patterns using backward trajectory modelling.

## 2. Methodology

### 2.1 Field work

Five of the six firn cores (OH-7, OH-9, OH-10, OH-11 and OH-12) were drilled on LCL between 2014 and 2016. One core (LP-01) was retrieved from LP in 2016 (Fig. 1, Table 1). Cores OH-7 and OH-9 were obtained using a mechanical 9 cm diameter drilling device (Rufli auger; Fernandoy and others, 2012). All other cores were drilled using a portable solar-powered and electrically operated ice-core drill (Backpack Drill; icedrill.ch AG). The cores OH-7, OH-9 and OH-10 were collected at almost the same location, while OH-12 was recovered ~500 m further east and OH-11 ~1.5 km further southeast (Supplementary Fig. S1). The drill site of LP-01 is located ~250–300 m higher compared to the LCL cores. The cores were stored at the Chilean Antarctic Station Professor Julio Escudero on King George Island, South Shetland Islands, and then shipped for further processing to the Alfred Wegener Institute, Helmholtz Centre for Polar and Marine Research (AWI) in Bremerhaven, Germany, or the Universidad Nacional Andrés Bello (UNAB) in Viña del Mar, Chile.

### 2.2 Laboratory analyses

Firn cores OH-9, OH-10 and OH-12 were already analysed for their density and stable water isotope composition by Fernandoy and others (2018) and Hoffmann-Abdi and others (2021a), respectively. In addition to the pre-existing data (Fernandoy and others, 2017; Hoffmann-Abdi and others, 2021b), density profiles of cores OH-7 and LP-01 were obtained at the AWI in Bremerhaven using X-ray microfocus computer tomography with a measurement resolution of <1 mm (ICE-CT; Freitag and others, 2013). Subsequently, the two cores were subsampled at 0.05 m resolution and analysed for their stable water isotope composition at the ISOLAB Stable Isotope Facility of the AWI in Potsdam, Germany. The measurements were performed with cavity ring-down spectrometers L2130-*i* and L2140-*i* (Picarro Inc.) coupled to auto-samplers (L2130-*i*: PAL HTC-xt, CTC Analytics AG; L2140-*i*: Picarro Autosampler, Picarro Inc.). For each sample, six repeated injections were used, from which the first three were discarded. Raw data correction for linear drift and memory effects was carried out according to van Geldern and Barth (2012). Subsequently, the data were calibrated by linear regression using four different in-house standards that have been calibrated to the international VSMOW2 (Vienna Standard Mean Ocean Water)/SLAP2 (Standard Light Antarctic Precipitation) scale (Gröning and others, 2007). Stable water isotope ratios are reported in per mil (‰) vs VSMOW2. Precision of the measurements is  $\pm 0.1\text{‰}$  for  $\delta^{18}\text{O}$  and  $\pm 0.6\text{‰}$  for  $\delta\text{D}$ .

Firn core OH-11 was processed at the UNAB. A density profile was constructed by section-by-section determination of the core volume and weight resulting in an average resolution of 0.31 m.

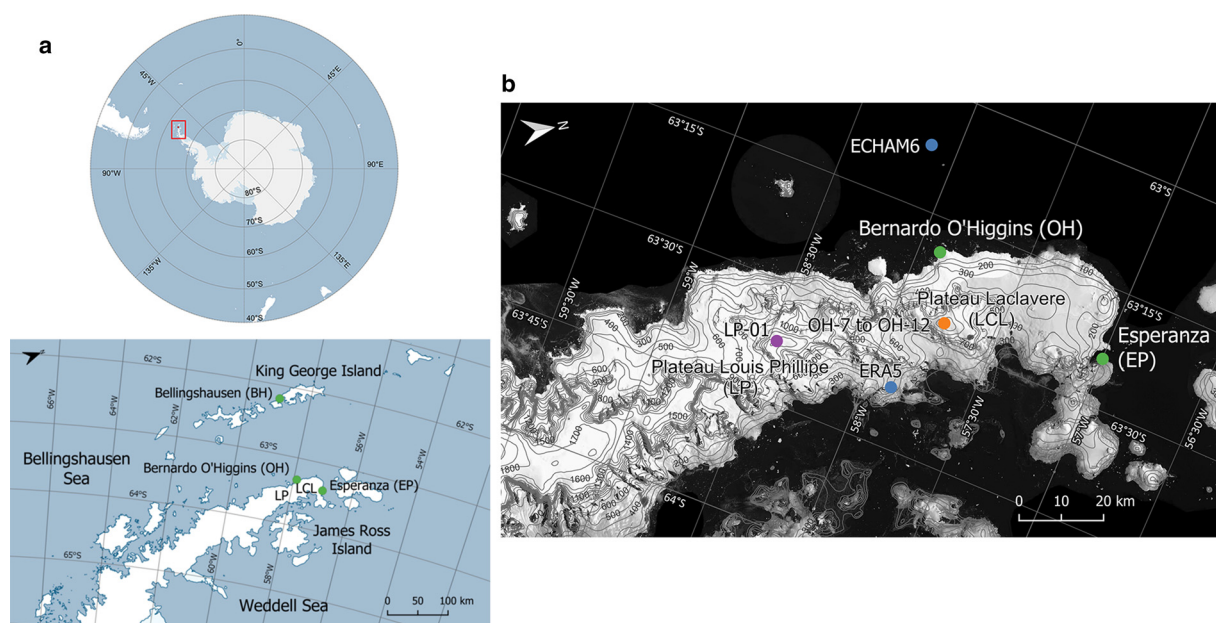


**Figure 1.** (a) Overview of the study area and (b) location of the drill sites of all firn cores retrieved from Plateau Laclavere (LCL; OH-7 to OH-12) and from Plateau Louis Phillippe (LP; LP-01) on the northern Antarctic Peninsula between 2014 and 2016. Green dots indicate the location of the Antarctic stations Bernardo O'Higgins (OH), Bellingshausen (BH) and Esperanza (EP). Blue dots mark the location of the ERA5 and ECHAM6-wiso grid points closest to the OH-12 drill site on LCL. Coordinates and altitudes of OH, BH and EP stations as well as of the ERA5 and ECHAM6-wiso grid points are given in Supplementary Table S1 (figure modified from Hoffmann-Abdi and others, 2021a).

The core was then subsampled at 0.05 m resolution for stable water isotope analysis carried out at the UNAB Stable Isotope Laboratory (LAI). Measurements were conducted with an off-axis integrated cavity output spectrometer (TLWIA 45EP; Los Gatos Research) using ten repeated injections for each sample, from which the first four were discarded. Each sample was measured twice on different days. Raw data were processed with the software LIMS (Laboratory Information Management System; Coplen and Wassenaar, 2015), which includes correction for linear drift and memory effects and subsequent normalization to the VSMOW2/SLAP2 scale (Gröning and others, 2007). Data normalization was done using three calibrated in-house standards and one international USGS standard (USGS49). Precision of the measurements is  $\pm 0.1\text{‰}$  for  $\delta^{18}\text{O}$  and  $\pm 0.8\text{‰}$  for  $\delta\text{D}$ .

For all cores, the d-excess ( $d\text{-excess} = \delta\text{D} - 8 \cdot \delta^{18}\text{O}$ ; Dansgaard, 1964) was calculated based on the calibrated  $\delta^{18}\text{O}$  and  $\delta\text{D}$  values. The d-excess is considered an indicator of the conditions in the moisture source region. Accordingly, the d-excess for water vapour evaporating from the ocean decreases as relative humidity increases and sea surface temperature decreases (Merlivat and Jouzel, 1979; Uemura and others, 2008; Pfahl and Sodemann, 2014).

Firn core OH-9 was analysed for chemical impurities at the Ice Chemistry Laboratory of the British Antarctic Survey (BAS) in Cambridge, UK (Supplementary Table S2). Major ions ( $\text{Cl}^-$ ,  $\text{Br}^-$ ,  $\text{F}^-$ ,  $\text{NO}_3^-$ ,  $\text{SO}_4^{2-}$ ,  $\text{Na}^+$ ,  $\text{K}^+$ ,  $\text{Mg}^{2+}$ ,  $\text{Ca}^{2+}$ ) and methane sulfonic acid (MSA) were determined using a Dionex reagent-free ion chromatography system (ICS-2000). Furthermore, hydrogen peroxide ( $\text{H}_2\text{O}_2$ ) was measured on the BAS Continuous Flow

Analysis (CFA) system following the methods in Grieman and others (2022).

Firn core OH-12 was additionally analysed in very high resolution (better than 10 mm) on the CFA system of the Trace Chemistry Laboratory of the Desert Research Institute (DRI) in Reno, Nevada, USA, according to methods described by Röthlisberger and others (2000) and McConnell and others (2002, 2007). In total, more than 20 chemical elements were measured using two Thermo Finnigan Element2 High Resolution-Inductively Coupled Plasma-Mass Spectrometry (HR-ICP-MS) instruments (Supplementary Table S2). Here we use previously published data on concentrations of black carbon (BC; Hoffmann-Abdi and others, 2021c), an indicator of biomass burning (Bond and others, 2007; McConnell and others, 2007), and sea-salt sodium ( $\text{ssNa}^+$ ; Hoffmann-Abdi and others, 2021d), along with measurements of other sea salt tracers, including  $\text{Ca}^{2+}$ ,  $\text{Sr}^{2+}$  and  $\text{Cl}^-$ , and mineral dust tracers, i.e. rare earth elements (REEs) such as Dy, Ce and La (Gabielli and others, 2010; Wegner and others, 2012).

### 2.3 Firn-core dating

For firn core OH-12, an age model was constructed by Hoffmann-Abdi and others (2021a). Cores OH-9 and OH-10 have previously been dated by Fernandoy and others (2018) based on similarities in the seasonal variability of measured firn-core d-excess profiles and d-excess time series synthetically derived from meteorological observations. However, since

**Table 1.** Details on drill locations of the six firn cores retrieved from the northern Antarctic Peninsula in 2014, 2015 and 2016

Firn core	OH-7	OH-9	OH-10	OH-11	OH-12	LP-01
Coordinates	63°27'13.2"S 57°45'22.8"W	63°27'09.9"S 57°45'21.4"W	63°27'09.7"S 57°45'21.6"W	63°27'22.2"S 57°46'41.6"W	63°27'25.0"S 57°45'14.5"W	63°37'26.0"S 58°27'45.8"W
Altitude (m a.s.l.)	1130	1130	1130	1130	1090	1388
Depth (m)	15.31	11.65	10.17	20.44	19.93	21.38
Drilling date	24/01/2014	28/01/2014	25/01/2015	28/01/2015	14/01/2016	14/01/2016

Hoffmann-Abdi and others (2021a) suggested that the age models of these cores contain a dating error of +1 year, we did not use them. Instead, we re-dated OH-9, for which high-resolution glacio-chemical data are available, by applying annual layer counting (ALC) to the  $\text{H}_2\text{O}_2$  profile and confirming the results with measurements of MSA (Fig. 2a). Details on the ALC-procedure applied to OH-9 are provided in the Supplementary Method S1. The ALC-based age model comprises two full years, 2012 and 2013, with an estimated dating uncertainty ranging between  $\pm 1$  month in the upper part of the core and  $\pm 5$  months in the bottom section (Fig. 2a; Supplementary Method S1). To further improve the ALC-based age model of OH-9, we accounted for precipitation intermittency at the study site following the method previously employed for OH-12 (for details see Hoffmann-Abdi and others, 2021a; Supplementary Fig. S2). The precipitation-weighted age scales of OH-9 and OH-12 (Fig. 2b) are then used for inter-comparison of isotopic and glacio-chemical records and for statistical analysis. We use OH-12 as reference core because it covers the longest period and its age model is

the most sophisticated. The other cores, including OH-10, remain undated for this study.

#### 2.4 Datasets and data analysis

Based on the density measurements of OH-9 and the derived age model, annual snow accumulation rates were calculated and compared to those obtained from OH-12 (Hoffmann-Abdi and others, 2021a). Density profiles and calculated accumulation rates along with meteorological data (local near-surface air temperature, surface pressure) were then used to model depth-dependent diffusion lengths for each of the six firn cores across their entire length following the approach described by Münch and Laepple (2018) and Laepple and others (2018), respectively. For OH-10 and OH-11, high-resolution density profiles were calculated using the Herron–Langway model (Herron and Langway, 1980). Mean annual snow accumulation for the undated cores from LCL (OH-7, OH-10, OH-11) was assumed to equal the mean value derived from OH-9 and OH-12. For LP-01, the same accumulation rate as calculated for OH-12 was used due

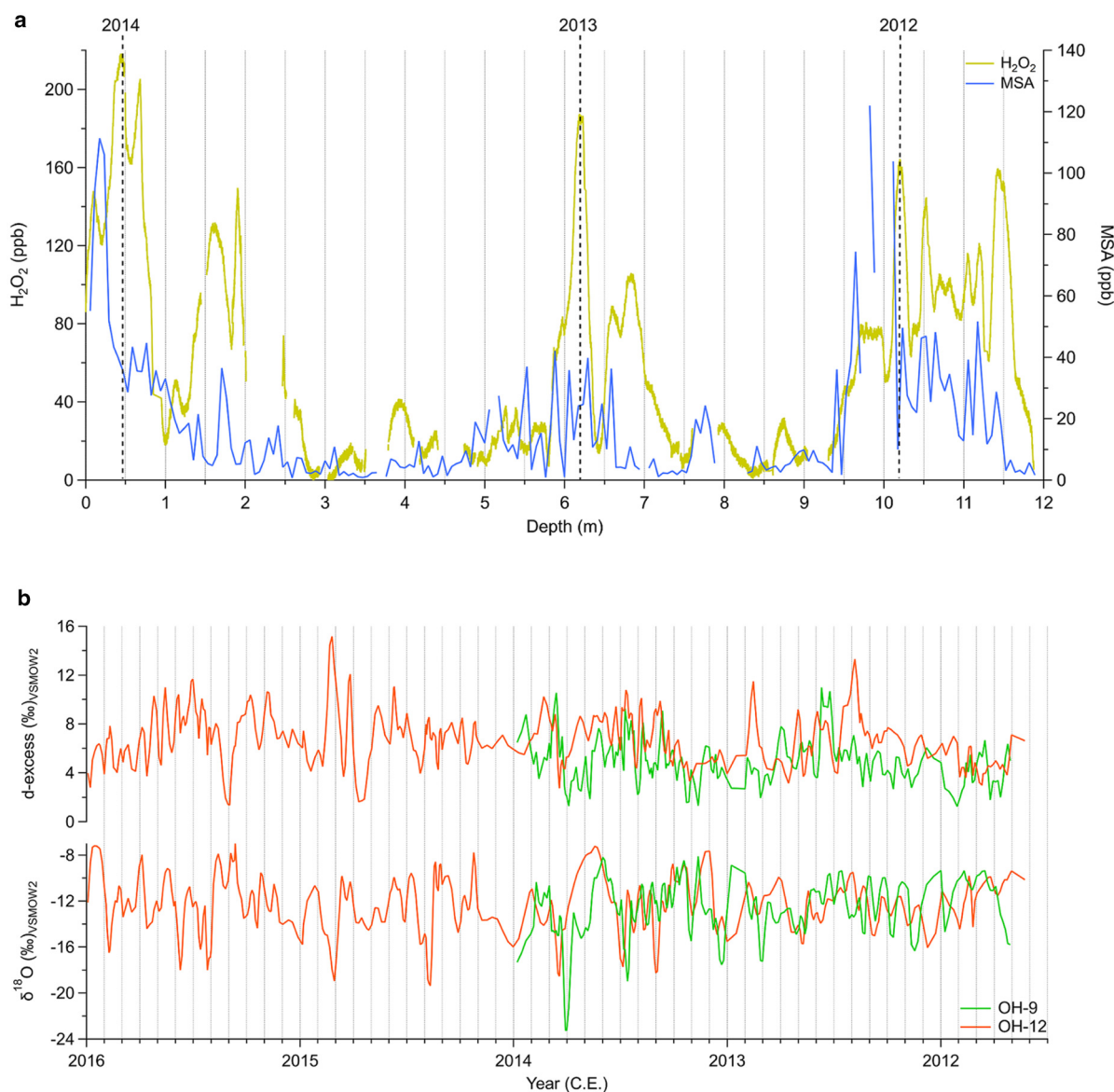


**Figure 2.** (a) Age model construction of firn core OH-9 based on annual layer counting applied to the high-resolution  $\text{H}_2\text{O}_2$  record (yellow) supported by the record of MSA (blue). (b) Comparison of  $\delta^{18}\text{O}$  and d-excess records of firn cores OH-9 (green) and OH-12 (orange) based on their weighted age scales. The weighted age scale of OH-12 was derived by Hoffmann-Abdi and others (2021a).

to the strong similarities between the density profiles of the two cores (see section 3.1). There are no long-term meteorological measurements available for LCL and LP. Therefore, local surface air pressure at the firn-core drill sites was calculated using the barometric height formula. Local near-surface air temperatures were estimated from near-surface air temperature and radiosonde measurements carried out at Bellingshausen station (BH), King George Island, between 1970 and 1998. The data were obtained at monthly resolution from the Reference Antarctic Data for Environmental Research (READER) database of the Scientific Committee on Antarctic Research (SCAR). Monthly mean lapse rates were calculated from the temperature and height difference between BH station (16 m a.s.l.) and the 850 hPa surface, excluding years with data gaps. Monthly mean near-surface air temperatures at the firn-core drill sites were then estimated from BH monthly mean near-surface air temperatures using the altitude of the respective site and the monthly mean lapse rates. To account for the distance between BH station and LCL and LP, respectively, BH temperatures were corrected by a value of  $-1.4$  °C. This is the mean temperature offset between BH and OH stations, whose near-surface air temperature records are highly correlated (Fernandoy and others, 2012, 2018; Hoffmann-Abdi and others, 2021a). Finally, annual mean near-surface air temperatures were estimated for each firn-core drill site based on the altitude- and distance-corrected monthly mean values.

Moreover, daily near-surface air temperature and precipitation records from Esperanza (EP), BH and OH stations were used for comparison with stable water isotope time series. The data are available from the Global Surface Summary of the Day (GSOD) of the National Centers for Environmental Information (NCEI). Due to data gaps in the observations, we also used data from the European Centre for Medium-Range Weather Forecasts (ECMWF) ERA5 Reanalysis (1979 onwards, spatial resolution: 31 km, temporal resolution: 1 h; Hersbach and others, 2020). ERA5 reanalysis data on daily near-surface and 850 hPa air temperatures and precipitation were extracted through the KNMI Climate Explorer. Near-surface air temperatures were corrected for the difference in elevation between firn-core drill sites and ERA5 grid points (Supplementary Table S1) on the basis of daily lapse rates calculated from the ERA5 near-surface and 850 hPa air temperature records (cf. Hoffmann-Abdi and others, 2021a).

Monthly data on Antarctic sea ice extent (SIE) were obtained from the National Snow and Ice Data Center (NSIDC). The Marshall SAM Index (MSI) at monthly resolution (Marshall, 2003) was employed to assess a possible connection between changes in the prevailing SAM phase and firn-core isotopic signals on a sub-annual scale. In addition, we used monthly time series of the ASL latitudinal and longitudinal position and the ASL Actual Central Pressure Index Version 3, which is defined as the pressure at the ASL location (Hosking and others, 2016). We further included seasonal time series of the latitude and strength of the circumpolar belt of tropospheric westerly winds over the Southern Ocean (Bracegirdle, 2018; Bracegirdle and others, 2018).

Statistical analysis of the used datasets comprised the calculation of Pearson correlation coefficients ( $r$ ) and  $p$ -values ( $p$ ) at the 95% confidence level (i.e.  $\alpha = 0.05$ ) and the estimation of signal-to-noise ratios following the approach of Fisher and others (1985).

### 2.5 ECHAM6-wiso and backward trajectory modelling

To validate the representativeness of firn-core isotopic signals with respect to atmospheric circulation, we compared them with simulations of the ECHAM6-wiso model nudged to ERA5

reanalyses. For this, data from grid points south of 40°S were extracted ( $\delta^{18}\text{O}$ ,  $\delta\text{D}$ , precipitation, 2 m-air temperature, surface temperature). ECHAM6-wiso is an isotope-enhanced version of the sixth generation of the atmospheric general circulation model ECHAM, developed by the Max Planck Institute for Meteorology in Hamburg, Germany (Stevens and others, 2013). A detailed description of the implementation of stable water isotopes in the ECHAM6 model as well as of recent improvements to the model can be found in Cauquoin and others (2019) and Cauquoin and Werner (2021).

For the interpretation of firn-core isotopic signals, knowledge on possible moisture source regions and transport pathways of precipitating air masses reaching the study area is essential. Therefore, we calculated 5 d backward trajectories using the Hybrid Single Particle Lagrangian Integrated Trajectory (HYSPPLIT) model (Draxler and Hess, 1998; Stein and others, 2015; Rolph and others, 2017). The Global Data Assimilation System (GDAS) archives from the National Oceanic and Atmospheric Administration (NOAA)/National Centers for Environmental Prediction (NCEP) with a  $1^\circ \times 1^\circ$  spatial and 1 h temporal resolution were used as input data to the model. The coordinates of the OH-12 drill site (Table 1) were taken as initial point. This approach also applies to the LP-01 drill site, since the resolution of the input data is too coarse to resolve local differences in meteorological conditions at this scale. The location of the study area at the ice divide of the northern AP allows a meteorological connection to both its western and eastern sides (Hoffmann-Abdi and others, 2021a). Therefore, trajectories were calculated for all days with precipitation registered at OH or EP stations in 2013, the overlapping year of the six firn cores (see section 3.4). A minimum threshold of  $1 \text{ mm d}^{-1}$  was used to exclude any sea-spray-related precipitation events at these coastal stations. The model was initiated at 15 UTC, i.e. at 12 noon local time, using a data-based vertical velocity field. For comparability with previous studies on the northern AP (Fernandoy and others, 2012, 2018), we chose a starting height of 1500 m a.s.l. ( $\sim 850$  hPa), which is higher than the sampling sites and minimizes interferences from the underlying topography (Sinclair and others, 2010). In total, 122 trajectories were calculated, clustered and visualized for selected time intervals. Cluster analysis is based on the spatial variance of the trajectories, i.e. trajectories with minimum differences are grouped together, thus representing precipitation events with similar transport pathways. Details on the cluster analysis with HYSPPLIT are provided in Stein and others (2015).

## 3. Results

### 3.1 Firn-core density records

All firn cores exhibit a clear increase in density with depth, resulting from snow compaction and the metamorphosis of snow to firn (Supplementary Figs S3 and S4). Measured density profiles of OH-10 and OH-11 do not allow for more detailed analyses due to their coarse resolution (Supplementary Fig. S4). Visual comparison of the density-depth records of OH-7, OH-9, OH-12 and LP-01 reveals strong similarities between cores that were drilled in the same year, both in terms of absolute values and variability. This is statistically confirmed by high correlation coefficients with negligible  $p$ -values calculated for the full cores based on 10 cm means ( $r = 0.65$ ,  $p < 0.0001$  for OH-7 and OH-9;  $r = 0.84$ ,  $p < 0.0001$  for LP-01 and OH-12; Supplementary Table S3). The similarities between the density-depth records of OH-12 and LP-01 suggest similar snow accumulation rates for LCL and LP. The average value of  $2500 \text{ kg m}^{-2} \text{ a}^{-1}$  (2012–2015) as calculated from OH-12 (Hoffmann-Abdi and

others, 2021a) is confirmed by OH-9, from which a mean snow accumulation of  $2460 \text{ kg m}^{-2} \text{ a}^{-1}$  is obtained (2012–2013; Table 2). Independently derived accumulation rates for 2012 and 2013, the overlapping years of OH-9 and OH-12, differ by only 6–8% ( $180\text{--}190 \text{ kg m}^{-2} \text{ a}^{-1}$ ; Table 2). For all cores, diffusion lengths increase continuously with depth, reaching maximum values of 0.05–0.07 m on LCL and 0.06 m on LP.

### 3.2 Inter-annual isotopic variability

Mean  $\delta^{18}\text{O}$  and  $\delta\text{D}$  values are similar for the five firn cores drilled on LCL, ranging between  $-11.6\text{‰}$  (OH-11) and  $-12.9\text{‰}$  (OH-10) and between  $-88.8\text{‰}$  (OH-11) and  $-98.8\text{‰}$  (OH-10), respectively (Table 3). The mean d-excess varies between  $4.3\text{‰}$  (OH-11) and  $6.8\text{‰}$  (OH-12). For core LP-01, mean  $\delta^{18}\text{O}$  and  $\delta\text{D}$  values are up to  $2.5\text{‰}$  and  $16.6\text{‰}$  lower, respectively, but the mean d-excess is highest ( $7.1\text{‰}$ ). Surprisingly, LP-01 does not show the absolute minimum  $\delta$ -values despite higher altitude, but OH-9. Since  $\delta^{18}\text{O}$  and  $\delta\text{D}$  values of all cores are highly correlated ( $r > 0.99$ ,  $p < 0.0001$ ; Supplementary Fig. S5), we restrict the following (statistical) analyses to  $\delta^{18}\text{O}$  and the d-excess.

In general,  $\delta^{18}\text{O}$  and d-excess values show a strong variability across the entire depth of each core, but no clear seasonal cyclicity (Fig. 3a and Supplementary Fig. S6). Visual comparison of the profiles reveals a similar variability for cores drilled in the same year as well as for those drilled in different years. However, they are not statistically correlated. Furthermore, the two dated cores OH-9 and OH-12 show a similar  $\delta^{18}\text{O}$  sequence in June–

October 2013 with a maximum offset of about two weeks: two prominent minimum peaks enclose a broad maximum peak (Fig. 2b). This minimum–maximum–minimum (MMM-)pattern is found in all six  $\delta^{18}\text{O}$ -depth records (Fig. 3a). In particular, the  $\delta^{18}\text{O}$  maximum peak can be clearly identified in all cores due to a distinct three-step staircase-like shape on its upward side (from the bottom; Fig. 3a). In OH-7 and OH-9, the MMM-pattern is located at  $\sim 1\text{--}3.5$  m depth, in OH-10 and OH-11 at  $\sim 5.4\text{--}7.3$  m depth and in OH-12 and LP-01 at  $\sim 10.2\text{--}12.7$  m depth (Fig. 3a).

To investigate the isotopic signal preservation in the cores in more detail, we placed their  $\delta^{18}\text{O}$  records on the same depth scale using the section with the 2013 MMM-pattern as reference point. Accordingly, we (1) aligned the  $\delta^{18}\text{O}$ -depth records of OH-7, OH-9, OH-10, OH-11 and LP-01 to the  $\delta^{18}\text{O}$  profile of OH-12, and (2) normalized the  $\delta^{18}\text{O}$  values. The second distinct minimum of the MMM-pattern (from the bottom) was used as tie point for the alignment, as it can be unambiguously identified in all cores. The  $\delta^{18}\text{O}$  profiles of all cores have been shifted according to their offset to the corresponding minimum in OH-12 (Table 4). LP-01 had to be shifted to the left (negative axis) to align the minima, although it was drilled on the same day as OH-12. Therefore, after the alignment the upper part of LP-01 was rescaled. In all aligned and normalized  $\delta^{18}\text{O}$  records, the MMM-pattern is clearly visible (Fig. 3b). From bottom to top,  $\delta^{18}\text{O}$  values on average increase by  $9.6\text{‰}$  from the first minimum to the maximum peak and then decrease again by  $12.4\text{‰}$  (Table 4). OH-11 and LP-01, both drilled at different locations than the other cores, show the lowest variability within the MMM-pattern (Table 4).

Aligned and normalized d-excess records of the six cores (Fig. 3c) do not show as clear similarities as the  $\delta^{18}\text{O}$  profiles. However, OH-7, OH-9, OH-12 and LP-01 exhibit a distinct, OH-10 and OH-11 a less pronounced minimum peak (on average  $2.4\text{‰}$ ; Table 4) at about the depth of the second  $\delta^{18}\text{O}$  minimum of the MMM-pattern ( $10.6\text{--}10.8$  m; Fig. 3c). In contrast, no such coincidence with the d-excess is found for the first  $\delta^{18}\text{O}$  minimum in any of the cores. While the d-excess stays on a relatively constant level in the section containing the  $\delta^{18}\text{O}$  maximum ( $\sim 11\text{--}12$  m; Fig. 3c), in total it decreases by on average  $5.1\text{‰}$  from the first to the second  $\delta^{18}\text{O}$  minimum (Table 4).

Other similarities between the six cores within the overlapping part ( $9.4\text{--}15.3$  m depth in Fig. 3) are more difficult to identify.

**Table 2.** Annual accumulation rates calculated for the drill sites of firn cores OH-9 and OH-12 on LCL for the period 2012–2013 and 2012–2015, respectively

Firn core	OH-9	OH-12
Year	Accumulation rate ( $\text{kg m}^{-2} \text{ a}^{-1}$ )	Accumulation rate ( $\text{kg m}^{-2} \text{ a}^{-1}$ )
2012	2210	2390
2013	2710	2890
2014	–	2470
2015	–	2260
Annual mean	2460	2500

The OH-12 accumulation rates are from Hoffmann-Abdi and others (2021a).

**Table 3.** Basic statistics of the stable water isotope composition of the six firn cores of Table 1 with respect to the entire core depth (numbers without brackets) as well as to the depth interval from 9.8 m to 14.6 m, corresponding to the year 2013 in OH-12 (numbers in brackets)

Firn core	OH-7	OH-9	OH-10	OH-11	OH-12	LP-01
$\delta^{18}\text{O}$ (‰)						
Min	–20.3 (–20.3)	–23.3 (–23.3)	–21.9 (–21.1)	–19.7 (–18.7)	–19.4 (–18.5)	–19.7 (–19.7)
Mean	–12.3 (–12.6)	–12.8 (–13.0)	–12.9 (–12.6)	–11.6 (–11.5)	–12.4 (–12.4)	–14.1 (–14.2)
Max	–7.2 (–7.9)	–8.1 (–8.1)	–7.2 (–7.3)	–6.8 (–6.8)	–7.0 (–7.2)	–8.9 (–9.8)
Min–max	13.0 (12.4)	15.1 (15.1)	14.6 (13.9)	12.9 (11.9)	12.4 (11.3)	10.9 (9.9)
Sdev ( $\sigma$ )	2.2 (2.5)	2.5 (3.0)	2.6 (2.5)	2.2 (2.6)	2.4 (2.8)	2.1 (2.2)
$\delta\text{D}$ (‰)						
Min	–160.1 (–160.1)	–183.8 (–183.8)	–166.8 (–166.6)	–172.0 (–148.1)	–148.0 (–145.5)	–154.1 (–154.1)
Mean	–92.5 (–93.6)	–97.2 (–98.6)	–98.8 (–96.1)	–88.8 (–88.7)	–92.0 (–92.6)	–105.4 (–106.5)
Max	–52.6 (–56.5)	–59.6 (–59.6)	–55.8 (–55.8)	–49.8 (–52.3)	–49.3 (–49.3)	–63.7 (–69.7)
Min–max	107.5 (103.7)	124.2 (124.2)	111.0 (110.8)	122.3 (95.7)	98.7 (96.2)	90.4 (84.5)
Sdev ( $\sigma$ )	17.8 (20.4)	20.4 (24.0)	20.4 (20.6)	17.9 (21.0)	19.2 (22.4)	16.9 (18.2)
d-excess (‰)						
Min	1.8 (1.8)	1.2 (1.3)	–6.5 (–2.9)	–6.6 (–1.6)	1.4 (2.7)	2.4 (3.6)
Mean	6.1 (6.8)	5.1 (5.4)	4.7 (4.5)	4.3 (3.3)	6.8 (6.9)	7.1 (7.4)
Max	12.5 (11.5)	11.0 (10.5)	11.3 (8.8)	16.2 (7.9)	15.2 (10.8)	11.6 (10.6)
Min–max	10.7 (9.7)	9.7 (9.2)	17.8 (11.7)	22.8 (9.5)	13.8 (8.0)	9.2 (6.9)
Sdev ( $\sigma$ )	1.9 (2.0)	1.9 (2.0)	2.7 (2.0)	3.2 (1.8)	2.1 (1.8)	1.8 (1.5)
n (samples)	313 (97)	232 (96)	190 (88)	408 (96)	414 (99)	425 (96)

Statistics for the 2013 depth interval were calculated based on depth-aligned records. Details on the depth alignment are given in the text.

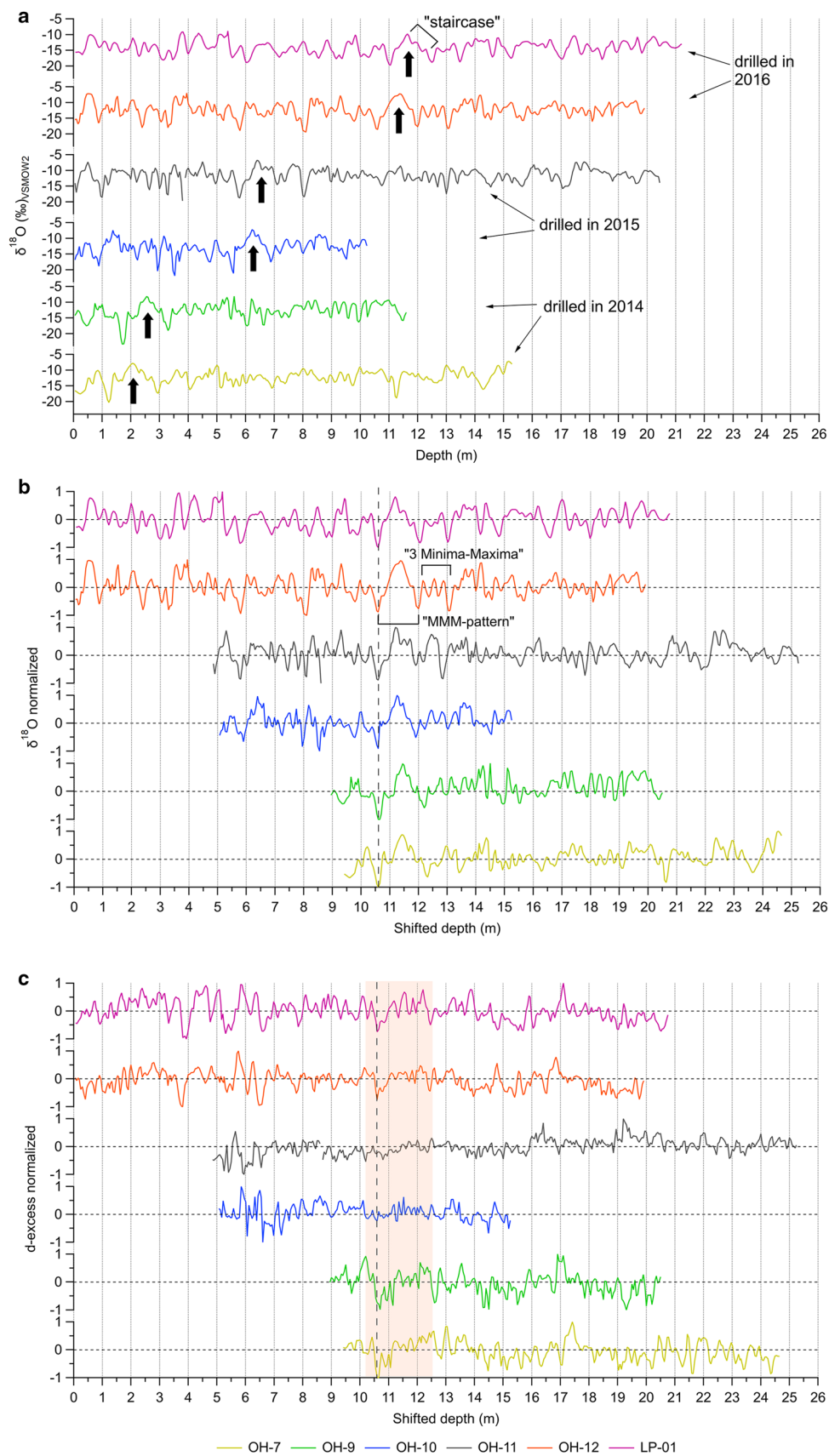


**Figure 3.** (a)  $\delta^{18}\text{O}$  profiles of the six firn cores of Table 1 with the year of drilling and the prominent minimum–maximum–minimum (MMM-)pattern indicated. The staircase-like shape on the upward side (from the bottom) of the  $\delta^{18}\text{O}$  maximum is marked for LP-01 as an example. (b–c) Depth-aligned and normalized  $\delta^{18}\text{O}$  and d-excess profiles of the six firn cores with OH-12 serving as the reference core. The  $\delta^{18}\text{O}$  minimum in OH-12 at 10.6 m depth, which was used as tie point for the alignment, is marked (vertical dashed line). In (b), the MMM-pattern and the preceding sequence of three minima and maxima are indicated for OH-12 as an example. In (c), the depth interval of the  $\delta^{18}\text{O}$  MMM-pattern (10.2–12.5 m) is highlighted.

**Table 4.** Depth and stable water isotope values of the MMM-pattern for each of the six firn cores of Table 1

Firn core	OH-7	OH-9	OH-10	OH-11	OH-12	LP-01	Mean
<b>Minimum I (June/July 2013)</b>							
Depth (m)	2.95	3.30	6.88	7.10	12.00	12.50	–
$\delta^{18}\text{O}$ (‰)	–17.4	–19.0	–17.5	–14.5	–17.7	–18.8	–17.5
$\delta\text{D}$ (‰)	–131.4	–143.7	–134.0	–111.1	–132.6	–142.0	–132.5
d-excess (‰)	7.6	8.0	6.4	5.0	9.1	8.6	7.5
<b>Maximum (August 2013)</b>							
Depth (m)	2.05	2.55	6.23	6.40	11.37	11.64	–
$\delta^{18}\text{O}$ (‰)	–7.9	–8.2	–7.2	–6.8	–7.2	–9.8	–7.9
$\delta\text{D}$ (‰)	–56.5	–59.6	–55.8	–52.3	–49.3	–69.7	–57.2
d-excess (‰)	6.4	5.9	2.2	2.0	8.6	8.8	5.7
<b>Minimum II (October 2013)</b>							
Depth (m)	1.23	1.70	5.58	5.80	10.60	11.05	–
Offset to OH-12 (m)	9.37	8.90	5.02	4.80	0	–0.45	–
$\delta^{18}\text{O}$ (‰)	–20.3	–23.3	–21.1	–18.7	–18.5	–19.7	–20.3
$\delta\text{D}$ (‰)	–160.1	–183.8	–166.6	–148.1	–145.5	–154.1	–159.7
d-excess (‰)	1.9	2.3	2.1	1.8	2.7	3.6	2.4
<b>Minimum I–Maximum</b>							
Distance (m)	0.90	0.75	0.65	0.70	0.63	0.86	0.75
$\delta^{18}\text{O}$ (‰)	9.5	10.8	10.3	7.7	10.5	9.0	9.6
$\delta\text{D}$ (‰)	75.0	84.1	78.2	58.8	83.3	72.4	75.3
d-excess (‰)	1.2	2.1	4.2	3.0	0.5	0.2	1.8
<b>Minimum II–Maximum</b>							
Distance (m)	0.82	0.85	0.65	0.60	0.77	0.59	0.71
$\delta^{18}\text{O}$ (‰)	12.4	15.1	13.8	11.9	11.3	9.9	12.4
$\delta\text{D}$ (‰)	103.7	124.1	110.8	95.7	96.2	84.5	102.5
d-excess (‰)	4.5	3.7	0.04	0.2	5.9	5.1	3.2

For the second minimum (from the bottom; Minimum II), the offset relative to the depth of the minimum in OH-12 is reported for each core. The difference between the first and second minimum (from the bottom; Minimum I and Minimum II), respectively, and the maximum peak is also given for each core.

From bottom to top, there is a sequence of three smaller  $\delta^{18}\text{O}$  minima and maxima preceding the MMM-pattern that can be seen in all cores (Fig. 3b). The sequence is most clearly pronounced in OH-10, OH-12 and LP-01 between 12 m and 13 m depth, while it is shifted by  $\sim 0.5$  m in OH-7 and OH-9 (Fig. 3b). Similar to the MMM-pattern, the  $\delta^{18}\text{O}$  minima are associated with d-excess minima in most cases.

In summary, the six firn cores reveal a similar MMM-pattern in their  $\delta^{18}\text{O}$  records, dated to austral winter/spring 2013 by two independent age models. This points towards (1) a prominent regional synoptic pattern, (2) excellent signal preservation and (3) reduced post-depositional processes. To investigate these aspects further, we chose the year 2013 as determined in OH-12, since the respective depth section (9.8–14.6 m) is fully contained in all cores.

### 3.3 Isotopic variability in 2013 (depth interval 9.8–14.6 m) and comparison with meteorological records

The basic statistics of the six firn cores for the depth interval 9.8–14.6 m are similar to those found for the entire records (Table 3). Std dev. for  $\delta^{18}\text{O}$ ,  $\delta\text{D}$  and the d-excess are generally low and show little variability among the cores (Table 3). LP-01 exhibits the lowest variability for  $\delta^{18}\text{O}$ ,  $\delta\text{D}$  and the d-excess in terms of the minimum–maximum range and std dev., whereas OH-9 varies the most (except for d-excess).

Furthermore, cross-correlation analysis based on 10 cm means reveals statistically significant positive values of about  $r = 0.4$  to  $r = 0.7$  for  $\delta^{18}\text{O}$  and  $\delta\text{D}$ , respectively, and about  $r = 0.3$  to  $r = 0.5$  for the d-excess ( $p < 0.05$  or lower; Supplementary Table S4). Correlations are highest between OH-10 and OH-12. LP-01 correlates well with all LCL cores for  $\delta^{18}\text{O}$  and  $\delta\text{D}$ , but for the d-excess a statistically significant correlation only exists with OH-9 and OH-12. In general, cores drilled in the same year are strongly and statistically significantly correlated for  $\delta^{18}\text{O}$ ,  $\delta\text{D}$  and the d-excess (Supplementary Table S4). The mean cross-correlation for all cores is  $\sim 0.5$  for both  $\delta^{18}\text{O}$  and  $\delta\text{D}$ , and 0.3

for the d-excess, resulting in signal-to-noise ratios of  $\sim 1.1$  for  $\delta^{18}\text{O}$  and  $\delta\text{D}$ , and 0.4 for the d-excess, respectively (Supplementary Table S5).

For comparison with meteorological records, we use firn core OH-12.  $\delta^{18}\text{O}$  time series and especially the prominent MMM-pattern have no equivalent in near-surface air temperature records for 2013 (Figs 4a, b), resulting in no statistical relationship (Supplementary Table S6). Instead, the broad  $\delta^{18}\text{O}$  maximum in July–September 2013 is associated with generally rather low temperatures at the site. Shifting the isotopic record relative to the temperature time series by  $\pm 2$  months, which corresponds to the dating uncertainty of OH-12 in this part of the core (Hoffmann-Abdi and others, 2021a), does not improve the correlation. However, the d-excess shows a statistically significant negative correlation with all temperature records ( $r < -0.7$ ,  $p < 0.01$ ; Supplementary Table S6).

Precipitation records from nearby stations (OH, BH, EP) and ERA5 reanalysis data for 2013 show that precipitation events occur throughout the year. This is typical for such a maritime location (cf. Turner and others, 2019). The highest frequency and amount of precipitation occurs during the transitional seasons and towards winter (Figs 4c–f). Contemporaneously, the d-excess record of OH-12 has its largest variability (March–June) with values ranging from 3.3‰ to 10.8‰. Conversely, during the winter and summer months, the d-excess stays on relatively constant levels (January–February and December:  $5.1 \pm 0.7$ ‰; July–September:  $7.6 \pm 1.1$ ‰; Fig. 4a). With respect to the MMM-pattern, the OH record shows extreme precipitation events, i.e. daily precipitation was much larger than the 90th percentile of the whole precipitation time series (1985–2021; cf. Turner and others, 2019), at around the time of the two  $\delta^{18}\text{O}$  minima in June/July and mid-October 2013, respectively (Fig. 4c). While the extreme precipitation event in July has no counterpart in other regional precipitation records, the one in October can also be identified in the BH and ERA5 precipitation records (Figs 4d, f). The period with the broad  $\delta^{18}\text{O}$  maximum and relatively constant d-excess values (mid-July–September) is



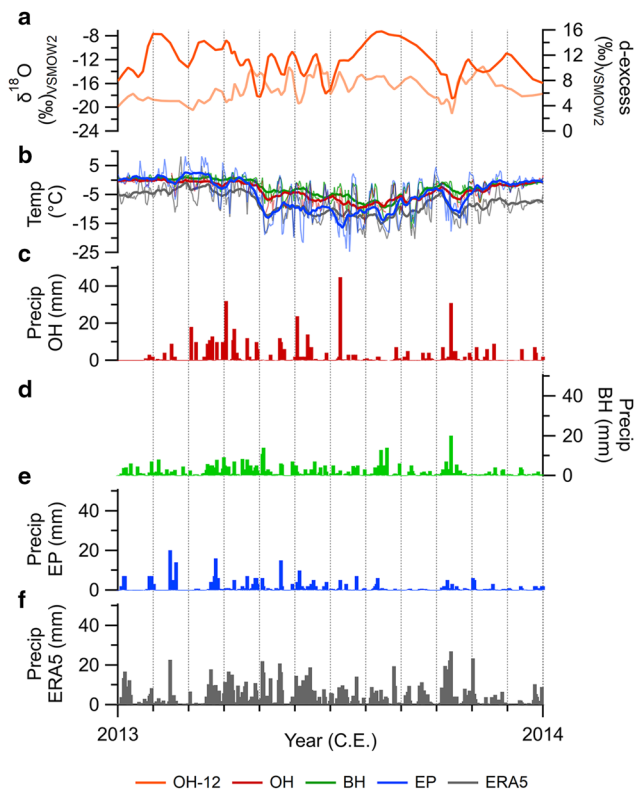


**Figure 4.** Time series of (a)  $\delta^{18}\text{O}$  (orange) and d-excess (light orange) of firn core OH-12 compared to the records of (b) near-surface air temperature and (c–f) daily precipitation from Bernardo O'Higgins (OH, red), Bellingshausen (BH, green) and Esperanza (EP, blue) stations as well as from the ERA5 gridpoint closest to the OH-12 drill site (grey; Fig. 1b and Supplementary Table S1) for the year 2013. For near-surface air temperatures, daily values (thin lines) as well as the 15-point-running mean (bold lines) are shown.

generally characterized by less frequent and small precipitation events (<10 mm) in the OH and EP records, while BH and ERA5 show precipitation events with up to 20 mm in mid and late August, respectively (Figs 4c–f).

### 3.4 Isotopic and backward trajectory modelling

The comparison between the  $\delta^{18}\text{O}$  and d-excess records of firn core OH-12 and the ECHAM6-wiso model reveals that modelled absolute values are on average  $\sim 1.9\text{‰}$  ( $\delta^{18}\text{O}$ ) and  $3.0\text{‰}$  (d-excess) lower than measured absolute values. However, the temporal variability is similar with an offset of about 1–2 months (Figs 5a, b). Especially, the  $\delta^{18}\text{O}$  MMM-pattern in 2013 is well reproduced by the ECHAM6-wiso model in terms of amplitude and timing (Fig. 5a). In 2012, the mismatch between measured and modelled records is larger (Figs 5a, b) which might be due to the higher dating uncertainty of OH-12 in the bottom part of the core (cf. Hoffmann-Abdi and others, 2021a). Therefore, the year 2012 was excluded from spatial cross-correlation analysis between measured and modelled isotopic data. For the period 2013–2015, correlations are observed for both  $\delta^{18}\text{O}$  and the d-excess (Figs 6a, b). Correlation coefficients generally increase from the eastern towards the western side of the AP for the d-excess (up to  $r \sim 0.5$ ,  $p < 0.05$ ; Fig. 6b). For  $\delta^{18}\text{O}$ , they also increase from east to west (up to  $r \sim 0.6$ ,  $p < 0.05$ ; Fig. 6a), but then decrease again. Furthermore, statistically significant positive correlations for  $\delta^{18}\text{O}$  are primarily confined to areas further southwest of the study site (Fig. 6a). In contrast, for the d-excess, they are observed in the Bellingshausen Sea, near and on the South American continent (Tierra del Fuego) and to a lesser extent in the Weddell Sea (Fig. 6b).

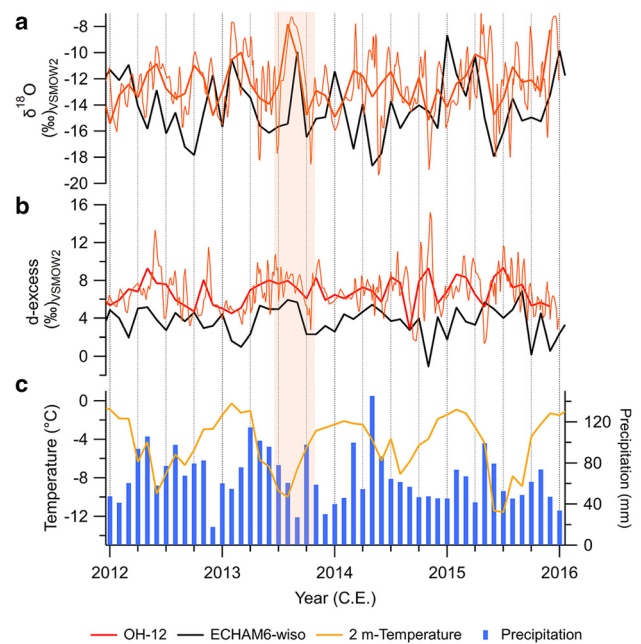


**Figure 5.** Comparison of high-resolution (thin orange lines) and monthly (bold orange lines) (a)  $\delta^{18}\text{O}$  and (b) d-excess records of firn core OH-12 with monthly  $\delta^{18}\text{O}$  and d-excess records produced by the ECHAM6-wiso model (black lines) for the gridpoint closest to the OH-12 drill site (Fig. 1b and Supplementary Table S1) for the period 2012–2015. In (c), the 2 m-air temperature (yellow line) and precipitation (blue bars) time series of the used ECHAM6-wiso gridpoint are shown. The period of the  $\delta^{18}\text{O}$  MMM-pattern in 2013 (June–October) is highlighted.

Similar observations are made when only the year 2013 is considered. Compared to the period 2013–2015, correlation coefficients for both  $\delta^{18}\text{O}$  and the d-excess are generally higher. This is also due to the reduced number of data points in the time series. Statistically significant ( $p < 0.05$ ) positive correlations for  $\delta^{18}\text{O}$  and the d-excess reach values of up to  $r \sim 0.7$  and  $r \sim 0.8$ , respectively (Figs 6c, d). The high d-excess correlations on the western side of the AP follow the westerly wind belt all the way from the Ross Sea (not shown).

Frequency and cluster analysis of 5 day backward trajectories for the overlapping year 2013 reveals a clear dominance of both short- (47%) and long-range (45%) western and southwestern transport pathways towards the northern AP (Figs 7a, c). Moisture advection from more northerly directions (South America, South Pacific Ocean) account for only 8% of all trajectories. With respect to the period of the MMM-pattern (June–October 2013), transport pathways of precipitating air masses additionally show a rather local eastern component (7%; Figs 7b, d). Furthermore, the percentage of trajectories originating over the South Pacific Ocean and passing by the South American continent is almost twice as high as in the entire year 2013 (15% instead of 8%).

## 4. Discussion

### 4.1 Validity of the firn-core alignment

The alignment of the six firn cores assumes that the prominent MMM-pattern identified in the  $\delta^{18}\text{O}$  profiles of all cores represents the same sequence of synoptic events and can therefore be used as a tie point to bring all cores on the same depth scale. Three aspects underpin this approach: First, the two independently derived age models of OH-9 and OH-12 both date the MMM-pattern to the same period (June–October 2013), suggesting a commonly preserved signal. Second, annual accumulation rates derived for LCL from OH-12 (Table 2) are in line with

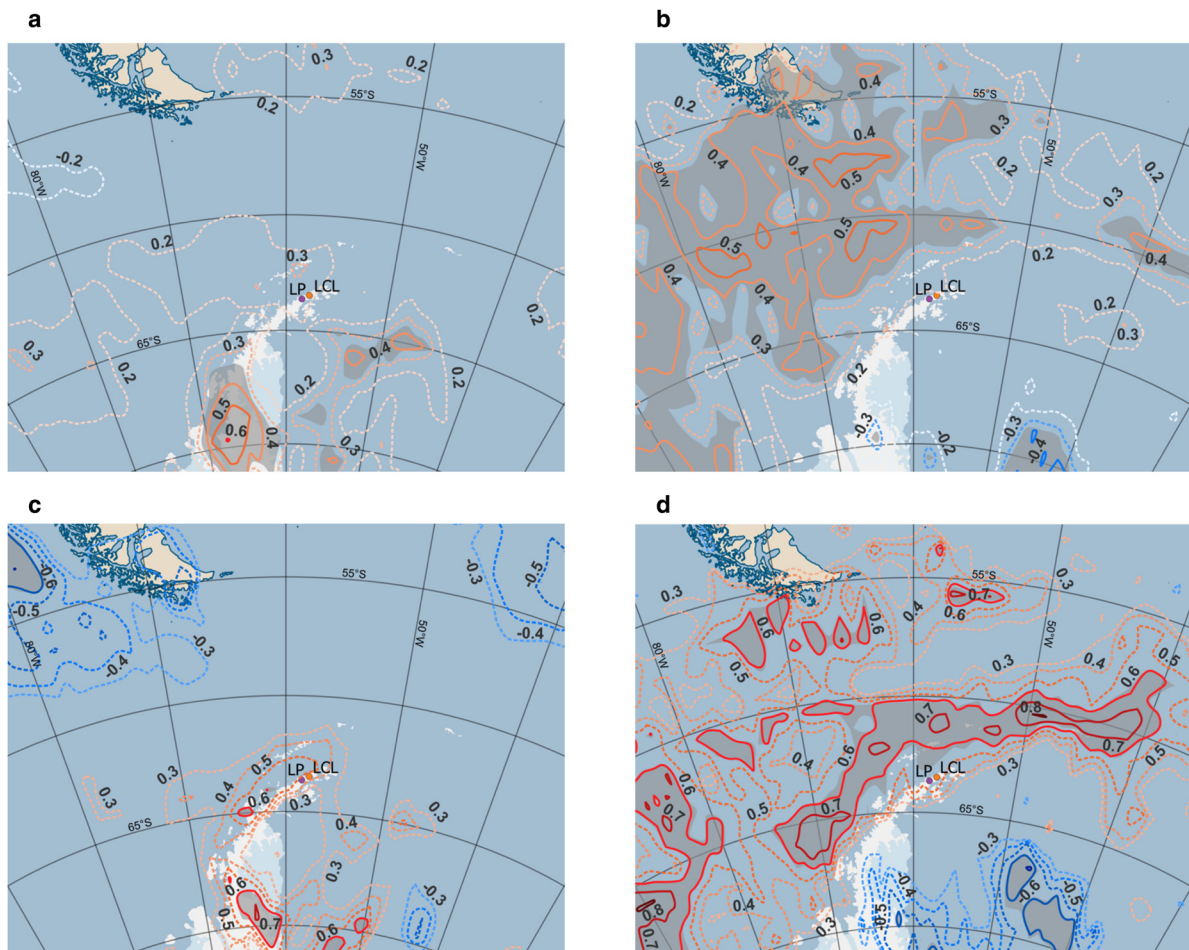


**Figure 6.** Contour maps of cross-correlations ( $r$ ) between isotopic records of firn core OH-12 and isotopic records produced by the ECHAM6-wiso model for grid points covering the northern Antarctic Peninsula and surrounding regions in the Bellingshausen and Weddell Seas as well as near the South American continent. (a) Cross-correlations for  $\delta^{18}\text{O}$  in the period 2013–2015; (b) cross-correlations for the d-excess in the period 2013–2015; (c) cross-correlations for  $\delta^{18}\text{O}$  in 2013; (d) cross-correlations for the d-excess in 2013. For the period 2013–2015 (a and b), only contour lines with  $r \geq +3$  or  $r \leq -3$  are shown. For the year 2013 (c and d) with generally higher correlation coefficients, only contour lines with  $r \geq +3$  or  $r \leq -3$  are displayed. Positive correlations are coloured from light to dark red with increasing  $r$ , negative correlations are coloured accordingly from light to dark blue. Contours of statistically significant correlations ( $p < 0.05$ ) are displayed as solid lines, contours of statistically non-significant correlations as dashed lines. In addition, statistically significant areas ( $p < 0.05$ ) are marked by grey shading. The orange and magenta dots mark the drill sites on Plateau Laclavere (LCL) and Plateau Louis Phillipe (LP), respectively.

expected depths of the MMM-pattern in the other LCL cores (Table 4) with different drilling dates. Firn cores drilled two years before OH-12 (OH-7 and OH-9) were shifted by  $\sim 4.9$ – $5.2$  m weq. and those drilled one year earlier (OH-10 and OH-11) by  $\sim 2.6$ – $2.8$  m weq. Taking snow compaction into account, this corresponds roughly to the mean annual snow accumulation of  $2500 \text{ kg m}^{-2} \text{ a}^{-1}$  (Table 2). The small negative depth offset of the MMM-pattern in core LP-01 relative to OH-12 points towards a slightly higher accumulation rate on LP than on LCL. Third, aligning the cores to the tie point generally improves cross-correlations between cores. This is valid for  $\delta^{18}\text{O}$  and  $\delta\text{D}$  (e.g.  $r$  increases up to  $>0.5$ ,  $p < 0.0001$ ; Supplementary Table S7), but also for the d-excess (e.g.  $r$  increases up to  $>0.4$ ,  $p < 0.0001$ ; Supplementary Table S7) and density (e.g.  $r$  increases from 0.65 to 0.75 for OH-7 and OH-9,  $p < 0.0001$ ; Supplementary Table S3).

In summary, the alignment to the second dated  $\delta^{18}\text{O}$ -minimum (October 2013) allows for synchronizing all six firn cores for the year 2013.

#### 4.2 Spatial and temporal preservation of isotopic signals

The strong visual similarities between aligned  $\delta^{18}\text{O}$ -depth records of firn cores drilled at different locations (e.g. LP-01 and OH-12)

and in different years (e.g. OH-9 and OH-12) suggest an excellent signal preservation at the regional scale and little alteration over time by post-depositional processes. This is also valid for the d-excess and is confirmed by the results of cross-correlation analysis (Supplementary Table S4).

High accumulation rates in the region facilitate the fast subsidence of freshly fallen snow and, hence, suggest water vapour diffusion to be reduced at the study site (Fernandoy and others, 2012, 2018; Hoffmann-Abdi and others, 2021a). In addition, high-density ice layers present in all cores may act as diffusion barriers (Fernandoy and others, 2018; Hoffmann-Abdi and others, ). Maximum diffusion lengths are much lower than the mean monthly layer thickness of the cores of  $\sim 0.4$  m, indicating that diffusive processes are likely confined to the month of snow deposition. Other near-surface post-depositional processes, such as isotopic exchange between the snowpack and atmospheric water vapour through condensation/sublimation (Ritter and others, 2016; Casado and others, 2021; Wahl and others, 2022), wind-forced firn ventilation (Neumann and Waddington, 2004; Town and others, 2008) and deep-air convection (Severinghaus and others, 2010) are also likely to be reduced or insignificant.

Surface melt can certainly affect the snowpack on LCL during the summer months (cf. Wille and others, 2019; Hoffmann-Abdi and others, 2021a). However, in the period of the MMM-pattern

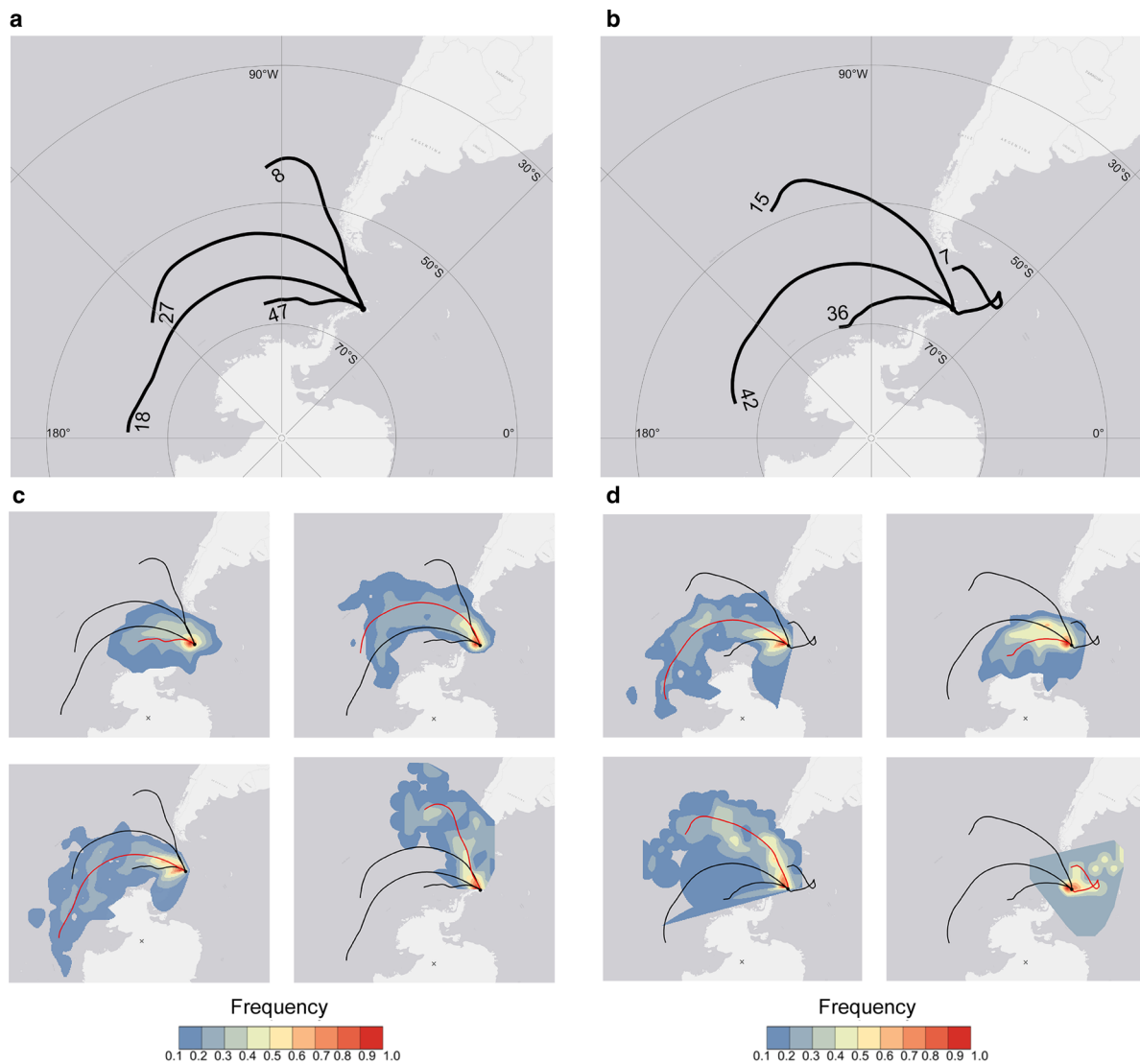


**Figure 7.** Results of cluster analysis of 5 d backward trajectories calculated for days with precipitation ( $\geq 1$  mm) registered at Bernardo O'Higgins and Esperanza stations in (a) 2013 and (b) during the period of the  $\delta^{18}\text{O}$  MMM-pattern (June–October 2013). The numbers are the percentage of the total number of trajectories calculated for 2013 ( $n = 122$ ) and June–October 2013 ( $n = 55$ ), respectively, for each cluster. In (c) and (d) the spatial frequency distribution of the trajectories grouping into each cluster, represented by the red trajectory, is shown for the two periods. The black dot in (a)–(d) indicates the location of the drill site of firn core OH-12, which was used as initial point for the backward trajectory modelling. The black cross in (c) and (d) marks the South Pole.

(June–October 2013) and in the following summer (2014), there are no melt layers present in the firn cores excluding isotopic modifications due to the infiltration, percolation and refreezing of surface meltwater (cf. Moran and others, 2011).

LCL and LP are both topographically flat plateaus that are exposed to high wind speeds all year round (Hoffmann-Abdi and others, 2021a). Therefore, wind drift is an important post-depositional process at the study site. It may alter or blur isotopic signals in the snowpack by removal, relocation and, thus, spatial admixing of isotopically different snow. This can lead to non-climate related variability in isotopic and glacio-chemical records of firn cores drilled at adjacent locations, so-called stratigraphic noise (Fisher and others, 1985; Münch and others, 2016, 2017). However, in the focus year 2013, wind drift appears to have had no recognizable influence on the isotopic composition of the snowpack at the study site. The  $\delta^{18}\text{O}$  MMM-pattern is clearly visible in all cores and has about the same amplitude. Differences in the spacing between the two minima of the MMM-pattern in the cores (Table 4) may be due to snow compaction.

The very good signal preservation is also reflected in the relatively high signal-to-noise ratios of  $\delta^{18}\text{O}$ ,  $\delta\text{D}$  and the  $d$ -excess for the 2013 depth interval (see section 3.3 and Supplementary Table S5). The calculated signal-to-noise ratios are in line with findings of Münch and Laepple (2018) for the West Antarctic Ice Sheet (WAIS), which is influenced by marine climate conditions likewise the AP but exhibits lower accumulation rates ( $< 500 \text{ kg m}^{-2} \text{ a}^{-1}$ ; Kaspari and others, 2004; Steig and others, 2005). The generally observed increase of signal-to-noise ratios with accumulation rates (Fisher and others, 1985; Steen-Larsen and others, 2011; Münch and others, 2016) additionally supports an excellent signal preservation at our study site. Münch and Laepple (2018) further point out that signal-to-noise ratios for the WAIS are inversely related to the timescale, i.e. they continuously decrease from values  $> 1$  at sub-annual timescales to  $\sim 0.5$ – $0.7$  at interannual and  $\sim 0.1$  at centennial timescales. Signal-to-noise ratios calculated for sub-annual to multiannual timescales at our study site (Supplementary Table S5) indicate the same dependence. However, a final conclusion cannot yet be drawn, as the common depth interval between at least two

cores only covers a maximum period of 3–4 years (e.g. OH-12 and LP-1).

### 4.3 Representativeness of preserved isotopic signals

Münch and others (2016) proposed sampling strategies to reduce stratigraphic noise, i.e. they recommend the excavation of at least five cores at a spacing of  $\geq 10$  m to obtain representative isotopic signals on the seasonal scale. These sampling strategies are fully met in this study. Moreover, their recommendations refer to low-accumulation areas ( $< 100 \text{ kg m}^{-2} \text{ a}^{-1}$ ; Münch and others, 2016). Hence, the high accumulation rates on the northern AP may further enhance the representativeness of the isotopic signals in the LCL and LP cores for local atmospheric conditions and specific synoptic situations occurring in the region (cf. Münch and others, 2016). This is supported by the highly similar temporal variability between firn-core and ECHAM6-wiso isotopic records (Fig. 5; see section 3.4). The slight temporal offset between measured and modelled data could result, on the one hand, from the dating uncertainty of OH-12 and, on the other hand, from the calculation of monthly mean values. The location of the OH-12 drill site (Table 1) at  $\sim 960$  m higher altitude compared to the nearest ECHAM6-wiso gridpoint (Supplementary Table S1) would imply lower  $\delta$ -values in the firn core than in the model. Hence, the observed opposite offset in absolute values is likely related to other factors than the elevation difference. A possible explanation might be inversion layers developing in the lower troposphere (up to 350–400 m a.s.l.) on the western side of the AP during months with sea-ice coverage (Fernandoy and others, 2018), inverting the vertical temperature-gradient. Furthermore, isotopic exchange between the snowpack and atmospheric water vapour allowing for secondary fractionation can lead to increased  $\delta$ -values in the snowpack (Casado and others, 2021; Hughes and others, 2021; Wahl and others, 2022). This process is not implemented in the ECHAM6-wiso model. In addition, incorrect moisture sources and transport pathways due to a mismatch between wind directions and strengths at the observation site and those used in the model (ERA5 wind fields) might account for the offset in absolute values (Bagheri Dastgerdi and others, 2021).

In the following, we investigate the relationship between firn-core isotopic signals, meteorological parameters and atmospheric circulation patterns.

### 4.4. Relation between firn-core isotopic signals and the regional meteorology on a sub-annual scale

#### 4.4.1 Relation to near-surface air temperatures and precipitation

Hoffmann-Abdi and others (2021a) discuss in detail the relationship between firn core stable water isotopes from LCL (using OH-12) and near-surface air temperatures from both nearby stations and ERA5 reanalysis data for the period 2012–2015. The d-excess was negatively related to ERA5 near-surface air temperatures, but no statistically significant correlation was found for  $\delta^{18}\text{O}$ . The same applies to the sub-annual scale as shown in this study (Supplementary Table S6). Similar observations were also made at other Antarctic coastal locations on inter-annual timescales (e.g. Masson-Delmotte and others, 2003; Vaughan and others, 2003; Goursaud and others, 2017, 2019). Previous studies in the region suggested several reasons for the de-coupling between condensation and near-surface air temperatures on LCL (Fernandoy and others, 2018; Hoffmann-Abdi and others, 2021a): (1) post-depositional processes such as wind drift, (2) the strongly maritime climate with reduced annual temperature amplitude and (3) the formation of inversion layers over sea-ice-covered areas on the western side of the AP in winter.

Precipitation records from nearby stations (OH, BH, EP) and ERA5 reanalysis data largely underestimate the precipitation amount on LCL due to the differences in altitude (Supplementary Table S1). Nevertheless, these datasets can provide some indication on the frequency, annual distribution and magnitude of precipitation events on LCL. The period of the MMM-pattern is characterized by an inverse relationship between stable water isotopes and precipitation. The two  $\delta^{18}\text{O}$  (and d-excess) minima of the MMM-pattern coincide with single extreme precipitation events while the maximum is associated with small to moderate, but more frequent precipitation events (Fig. 4). The same can be observed in most other months of 2013. These coincidences could be caused randomly by the dating uncertainty of OH-12. However, the  $\delta^{18}\text{O}$  record of ECHAM6-wiso for the OH-12 drill site shows the same behaviour in some parts, i.e. a coincidence of  $\delta^{18}\text{O}$  minima with precipitation maxima and vice versa (Fig. 5), pointing to the same inverse relationship.

From the above findings, we conclude that the isotopic composition of snow and firn on LCL and LP and its temporal variability may be determined by temporal changes in precipitation rather than air temperature. These in turn are likely to be linked to temporal changes in moisture sources and moisture transport pathways associated with specific synoptic situations. This is consistent with the results of Bagheri Dastgerdi and others (2021), who observed  $\delta^{18}\text{O}$  variations at Neumayer station (East Antarctica) related to changes in wind direction that occurred without contemporaneous changes in temperature.

#### 4.4.2 Moisture source variability

*Tracing moisture sources by backward trajectory modelling:* Backward trajectory modelling results for 2013 (Figs 7a, c) confirm findings of previous studies on moisture transport patterns for the northern AP region on interannual timescales, suggesting the circumpolar westerlies as their main agent (Fernandoy and others, 2012, 2018; Hoffmann-Abdi and others, 2021a). This is supported by the clear east–west-gradient of d-excess correlations between firn core OH-12 and the ECHAM6-wiso model on the (inter-)annual timescale (Figs 6b, d). On the sub-annual scale, moisture advection from directions other than the west can also be observed (Figs 7b, d), most likely due to changes in the strength, position and zonality of the circumpolar westerlies (see section *Transferability of identified isotopic and glacio-chemical fingerprints to other periods*). Statistically significant positive correlations between the OH-12 and ECHAM6-wiso d-excess records in the Weddell Sea and near the South American continent indicate that these regions may act as additional moisture sources for the study area (Fig. 6d).

At the time of the two  $\delta^{18}\text{O}$  minima of the MMM-pattern (June/July and mid-October 2013), a (north-)westerly flow pattern was dominant (Figs 8a, c), likely delivering high amounts of precipitation to the western side of the AP, as suggested by the OH precipitation record (Fig. 4b; section 4.4.1). During the period of the June/July minimum, precipitating air masses were transported over long distances across mainly ice-free areas of the Southern Ocean (Bellingshausen-Amundsen Sea, to a lesser extent Ross Sea) before reaching the study area (Fig. 8a). Hence, the gradual removal of heavy isotopes through condensation and precipitation along the transport pathway (Rayleigh distillation; Dansgaard, 1964; Rozanski and others, 1993), together with the orographic uplift at the mountain chain of the AP, could explain the low  $\delta^{18}\text{O}$  values. The same applies to the October minimum, however, precipitation events during that period occurred more frequently and the corresponding trajectories show a larger spatial spread (Fig. 8c). In addition to the western component, trajectories either crossed the South Pacific

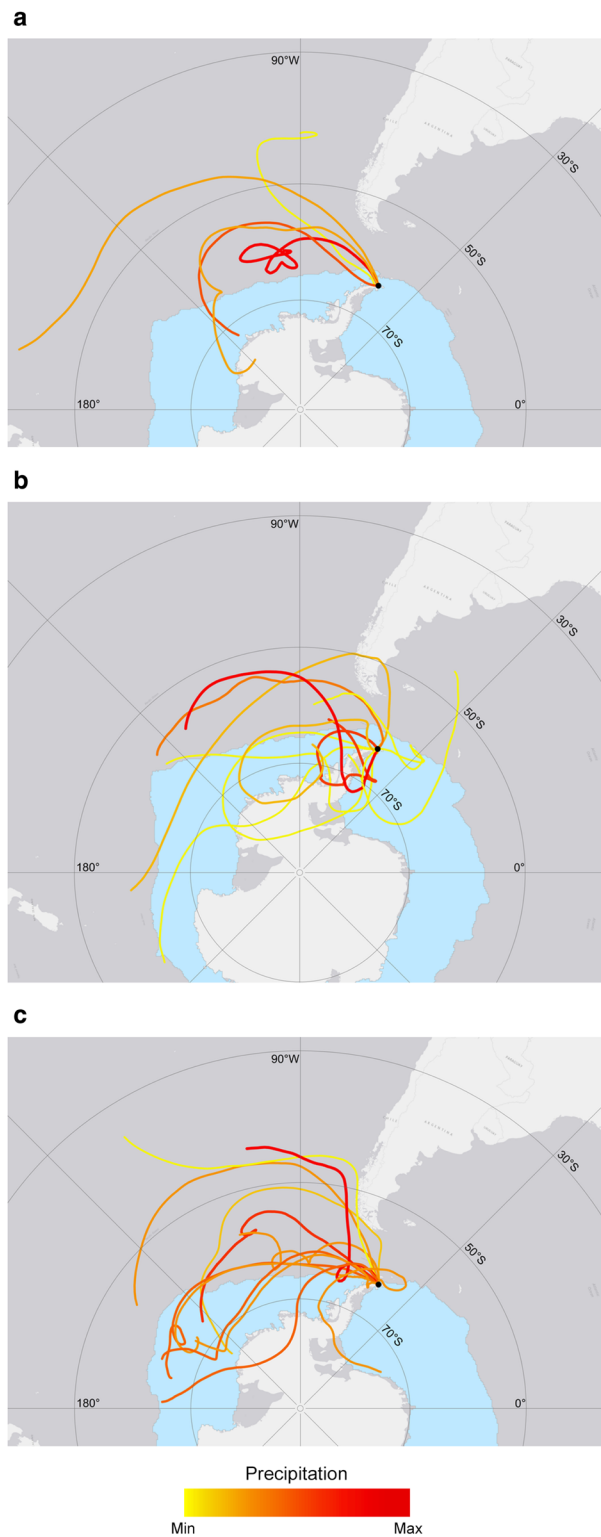


**Figure 8.** Five-day backward trajectories calculated for days with precipitation ( $\geq 1$  mm) registered at Bernardo O'Higgins (OH) and Esperanza (EP) stations at around the time of the three extrema of the  $\delta^{18}\text{O}$  MMM-pattern: (a) minimum in June/July 2013; (b) maximum in August 2013; (c) minimum in October 2013. Trajectories were ranked according to the amount of precipitation delivered (Supplementary Fig. S11) and then colour-coded from yellow (lowest rank) to red (highest rank). For days on which precipitation was recorded at both OH and EP stations, the higher precipitation amount was used for the ranking. The thickness of the trajectories increases as the amount of precipitation increases. The mean monthly sea ice extent for (a) July, (b) August and (c) October 2013 is shown in blue shading. The black dot in (a)–(c) indicates the location of the drill site of firn core OH-12, which was used as initial point for the backward trajectory modelling.

Ocean and passed the western coast of South America or they ran close to the Antarctic continent crossing ice-covered areas in the Ross Sea. The differences in the flow pattern between the two  $\delta^{18}\text{O}$  minima might be related to the seasonality of the polar vortex, which builds up in fall and breaks down in spring (Limpasuvan and Hartmann, 2000; Thompson and Solomon, 2002), allowing for stronger (weaker) westerly flow during the June/July (October) minimum (cf. Thompson and others, 2005; Black and McDaniel, 2007; Sheshadri and others, 2014). From backward trajectory modelling and regional precipitation records, we conclude that the  $\delta^{18}\text{O}$  minima are most likely related to the advection of maritime air masses towards the northern AP. Low d-excess values coinciding with the  $\delta^{18}\text{O}$  minima also indicate moisture origin from more southern oceanic regions (Stenni and others, 2010; Fernandoy and others, 2012).

Backward trajectory modelling results for the period of the  $\delta^{18}\text{O}$  maximum indicate that highest precipitation amounts were associated with trajectories originating either in the Bellingshausen-Amundsen Sea, similar to the  $\delta^{18}\text{O}$  minima, or in the vicinity of the northern AP (Fig. 8b). Goursaud and others (2019) suggest that moisture generated near the sea-ice margin may be associated with relatively high  $\delta^{18}\text{O}$  and d-excess values due to the short transport distance (limited Rayleigh distillation) and evaporation at low humidity levels (high kinetic fractionation). This is in line with our observations and supports the hypothesis of a larger contribution of locally derived moisture at the time of the  $\delta^{18}\text{O}$  maximum. High positive and statistically significant correlations between OH-12 and ECHAM6-wiso d-excess records found in the direct vicinity of the northern AP confirm the importance of proximal moisture for the study area (Fig. 6d). Furthermore, trajectories with a northern, i.e. South American component delivered considerable precipitation amounts, while trajectories from the Antarctic interior and the Weddell Sea yielded the least (Fig. 8b). In general, air masses transported from the Antarctic interior towards the AP (e.g. by katabatic winds) are cold and dry and would be associated with much lower  $\delta^{18}\text{O}$  and higher d-excess values (Masson-Delmotte and others, 2008; Goursaud and others, 2019) than observed in OH-12 (Table 3). Hence, the contribution of continental Antarctic moisture to the  $\delta^{18}\text{O}$  maximum was probably small. Trajectories from the Weddell Sea mostly crossed sea-ice-covered areas (Fig. 8b) with no evidence for the presence of open water (polynyas), which would have allowed for enhanced ocean-atmosphere heat and moisture transfer during that period (Haid and Timmermann, 2013; Mchedlishvili and others, 2022). Bonne and others (2019) demonstrated that snow accumulated on sea ice may act as an important moisture source in sea-ice-covered areas through sublimation, substantially influencing the isotopic composition of water vapour in the atmospheric boundary layer. Accordingly, with increasing sea-ice-coverage, d-excess values of water vapour and subsequent precipitation increase, while  $\delta^{18}\text{O}$  values decrease. However, in 2013, firn-core  $\delta^{18}\text{O}$  values clearly increased during the period of sea-ice coverage, which argues against snow on sea ice being a considerable moisture source at that time. In addition, stable water isotopes of snow samples collected on first- and second-year sea ice in the northwestern Weddell Sea exhibit mean values of  $-15.5\text{‰}$  for  $\delta^{18}\text{O}$ ,  $-122.2\text{‰}$  for  $\delta\text{D}$  and  $2\text{‰}$  for the d-excess (Arndt and others, 2021), which is much lower than those observed during the prominent  $\delta^{18}\text{O}$  maximum (Table 4). Hence, a connection of the  $\delta^{18}\text{O}$  maximum with air masses originating over South America or the South Pacific Ocean, in addition to locally derived moisture, is most likely. Previous studies on the northern AP

region (Fernandoy and others, 2012, 2018; Hoffmann-Abdi and others, 2021a) showed a clear link to the South American continent, especially in winter. Fernandoy and others (2012) combined backward trajectory modelling results with stable water isotope data of precipitation samples collected at OH station to investigate the relationship between the isotopic composition of precipitation events and the location of the moisture source. They showed that trajectories originating from or crossing the South American continent or the South Pacific Ocean are related to precipitation events with higher  $\delta^{18}\text{O}$  and lower d-excess values. The opposite is true for trajectories that pass over the Bellingshausen-Amundsen Sea. This confirms our findings for both the  $\delta^{18}\text{O}$  maximum and the two  $\delta^{18}\text{O}$  minima, although for the latter we observe low values also for the d-excess.

**Identifying moisture sources from glacio-chemical records:** Sea salt tracers in firn core OH-12, such as  $\text{ssNa}^+$ ,  $\text{Cl}^-$ ,  $\text{Ca}^{2+}$  and  $\text{Sr}^{2+}$ , exhibit local maxima ( $>1\sigma$ ) coinciding with both  $\delta^{18}\text{O}$  minima (Fig. 9b). This may point to moisture formed over sea-ice-free areas (cf. Goursaud and others, 2019), which is supported by the fact that mean monthly sea salt concentrations and Antarctic SIE show no statistically significant correlation on either annual (2013) or multiannual timescales (2012–2015; cf. Kreutz and others, 2000). In contrast, sea salt concentrations are low at the time of the  $\delta^{18}\text{O}$  maximum, suggesting moisture derived from near the sea-ice margin (cf. Goursaud and others, 2019).

The inverse relationship between  $\delta^{18}\text{O}$  and sea salt indicators is statistically corroborated by correlation coefficients of up to  $r$

$= -0.42$  ( $p < 0.05$ ), as calculated for the section of the MMM-pattern based on 10 cm means (Supplementary Table S8). Firn core OH-9 only shows a local maximum ( $>1\sigma$ ) in sea salt tracers during the October minimum (Supplementary Fig. S7), while no clear anti-correlation with  $\delta^{18}\text{O}$  exists (Supplementary Table S8). Instead, there is a statistically significant negative correlation between MSA and  $\delta^{18}\text{O}$  ( $r = -0.47$ ,  $p < 0.05$ ). The same relationship also holds for the d-excess ( $r = -0.51$ ,  $p < 0.05$ ; Supplementary Table S8). Accordingly, MSA values are low during the  $\delta^{18}\text{O}$  maximum and show a local maximum ( $>1\sigma$ ) during the October minimum, which is present in the d-excess as well (see section 3.2; Supplementary Fig. S7). Hence, we conclude that the  $\delta^{18}\text{O}$  (and d-excess) minima are likely associated with air masses originating from open ocean regions, while the  $\delta^{18}\text{O}$  maximum is partially related to locally generated moisture.

Moreover, the OH-12 high-resolution record of BC shows a local maximum ( $>2\sigma$ ) at the time of the  $\delta^{18}\text{O}$  maximum (Fig. 9c). In general, variations in BC concentrations primarily reflect changes in atmospheric transport patterns and source strength (Wolff and Cachier, 1998). Several studies have provided evidence for the transport of emissions from biomass burning in (tropical) South America, including forest fires, the burning of fossil fuels and bio-fuels, towards higher latitudes reaching as far as to the northern AP and Dronning Maud Land (e.g. Pereira and others, 2006; Fiebig and others, 2009; Jumelet and others, 2020; Liu and others; Hoffmann-Abdi and others, 2021a). In contrast, Cordero and others (2022) recently showed that local human activities, mainly research activities and tourism, can cause BC concentrations in Antarctic snow that are well above background levels ( $>1 \text{ ng g}^{-1}$ ). However, since the BC maximum in OH-12 occurs in winter, we consider such local sources to be unlikely.

Simultaneously to the BC maximum, elevated values ( $>1\sigma$ ) are also observed for REEs (Dy, La, Ce), which, however, are not the highest in the entire record (Supplementary Fig. S8). Provenance studies on REEs in ice cores have identified Patagonia as a major source of dust for Antarctica (Gaiero and others, 2004; Gabrielli and others, 2010; Wegner and others, 2012). There are no considerable local dust sources for the study site in winter, as almost all surrounding areas are snow-covered. Together with the generally low sea salt concentrations found in OH-12 concurrent with the  $\delta^{18}\text{O}$  maximum (Fig. 9b), this supports the hypothesis that the study area was also influenced by the advection of air masses from more northerly directions at that time in addition to locally derived moisture.

**Relation to large-scale atmospheric circulation:** As outlined above, the temporal variability of isotopic records seems to primarily reflect shifts in moisture sources and transport pathways of precipitating air masses. These in turn are related to temporal changes in the strength of the westerly flow prevailing in the region with a possible connection to the temporal variability of the SAM (Limpasuvan and Hartmann, 2000; Thompson and Wallace, 2000; Schmidt and others, 2007; Stenni and others, 2010). During the period of the MMM-pattern,  $\delta^{18}\text{O}$  values are inversely related to the MSI (Figs 9a, d), however, the correlation is not statistically significant ( $r = -0.7$ ,  $p = 0.2$ ). At the time of the two  $\delta^{18}\text{O}$  minima, the SAM entered a positive phase (MSI  $> 1$ ; Marshall and others, 2017) associated with a strengthening and southward shift of the circumpolar westerlies and a deeper and more easterly located ASL (Figs 9d, e). This likely favoured north-westerly flow across the AP region (cf. Hosking and others, 2013; Raphael and others, 2016), delivering high precipitation amounts and more sea salt aerosols (cf. Kreutz and others, 2000; Kaspari and others, 2005; Raphael and others, 2016) towards the study area, as confirmed by the results of backward trajectory modelling (Figs 8a, c) and the analysis of glacio-chemical records (see

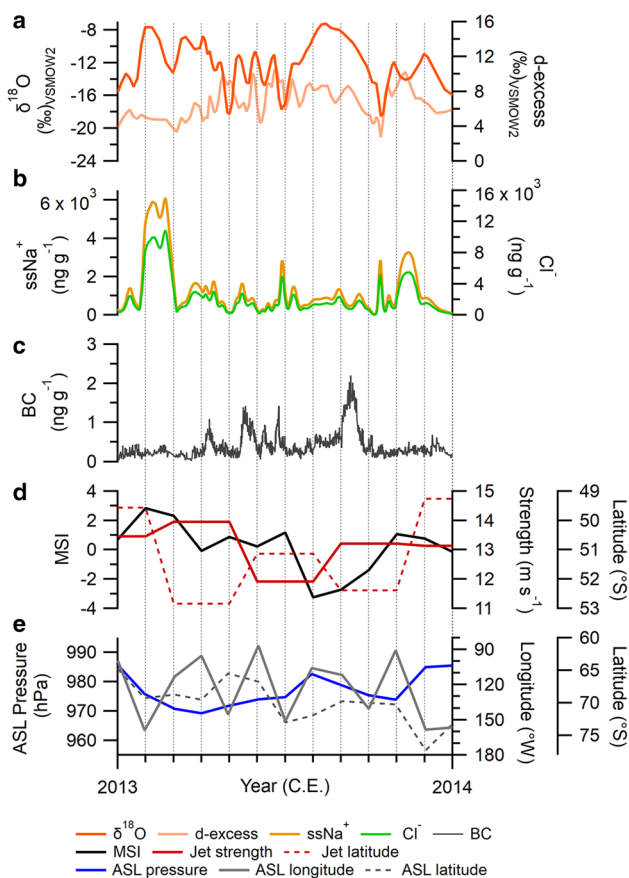


**Figure 9.** Time series of (a)  $\delta^{18}\text{O}$  (orange) and d-excess (light orange) of firn core OH-12 compared to OH-12 records of (b) sea-salt sodium ( $\text{ssNa}^+$ , dark yellow) and chlorine ( $\text{Cl}^-$ , green), (c) black carbon (BC, dark grey) and (d) the Marshall SAM Index (MSI, black), strength (red) and latitude position (dashed red) of the belt of tropospheric westerly winds over the Southern Ocean as well as (e) the Amundsen Sea Low (ASL) Actual Central Pressure Index Version 3 (blue), ASL longitude (grey) and latitude (dashed grey) position for the year 2013. Note that for the strength and latitude position of the westerly jet only seasonal means are available.

section *Identifying moisture sources from glacio-chemical records*). This is also consistent with the findings of Lubin and others (2008), who showed that a positive SAM in winter and spring increases the cyclonic activity in the Bellingshausen-Amundsen Sea and favours eastward trajectories. Consequently, extreme precipitation events are likely to occur more frequently on the western side of the AP (cf. Turner and others, 2019).

Conversely, during the period of the  $\delta^{18}\text{O}$  maximum, the SAM shifted into a strongly negative phase ( $\text{MSI} < -2$ ; Marshall and others, 2006). This was associated with a weakening and northward shift of the circumpolar westerlies and a weaker and more westerly located ASL (Figs 9d, e). On the AP, this generally leads to less extreme but more frequent smaller to moderate precipitation events (Turner and others, 2019), as observed in the regional precipitation records (Fig. 4). Furthermore, with a negative SAM in winter, the cyclonic activity in the Bellingshausen-Amundsen Sea decreases (Lubin and others, 2008), which could have favoured the transport of local moisture generated near the sea-ice margin towards the northern AP (cf. Goursaud and others, 2019). In addition, the stronger meandering of the circumpolar westerlies during negative SAM phases allows for air mass advection by meridional flow components either from the north (higher  $\delta^{18}\text{O}$ ) or from the south (lower  $\delta^{18}\text{O}$ ), as also indicated by the results of backward trajectory modelling (Fig. 8b).

*Transferability of identified isotopic and glacio-chemical fingerprints to other periods:* Relations between isotopic signals, glacio-chemistry and atmospheric circulation as observed for the MMM-pattern cannot be directly applied to other sections of the 2013 isotopic record. This is because the temporal variability of isotopic signals at the study site is not directly temperature-driven, but the result of a complex interplay between the prevailing synoptic situation, the location of moisture sources, air mass transport pathways and sea-ice conditions.

Nevertheless, for the sequence of three smaller  $\delta^{18}\text{O}$  (and d-excess) minima and maxima preceding the MMM-pattern (May–June 2013) and detectable in all six firn cores, we found the same connection between  $\delta^{18}\text{O}$  values and moisture transport pathways as discussed above (Supplementary Fig. S9). Accordingly, the  $\delta^{18}\text{O}$  minima are rather related to westerly wind-dominated transport pathways with the Bellingshausen-Amundsen Sea as primary moisture source. In contrast, the  $\delta^{18}\text{O}$  maxima show a clear link to the South American continent and to some extent to the Weddell Sea (Supplementary Fig. S9b). The sequence falls in a season with generally increased precipitation frequency (Fig. 4). Unlike the MMM-pattern, a clear assignment of single precipitation events to the  $\delta^{18}\text{O}$  minima and maxima is difficult due to the shortness of the period and the dating uncertainty of OH-12 ( $\pm 2$  months; Hoffmann-Abdi and others, 2021a). There are also no distinct correspondences between high/low  $\delta^{18}\text{O}$  values and chemical impurities.

It is challenging to identify further  $\delta^{18}\text{O}$  maximum and minimum peaks common to all six firn cores. In January and February 2013, OH-12 shows a distinct  $\delta^{18}\text{O}$  maximum (Fig. 9a), which is otherwise only clearly visible in LP-01 at a depth of 14–15 m (Fig. 3a). It is accompanied by relatively low d-excess values (Fig. 9a). Different from the MMM-pattern, the high  $\delta^{18}\text{O}$  values coincide with a remarkable maximum in the sea salt indicators ( $> 2\sigma$ ; Fig. 9b), suggesting moisture transport across open ocean areas (cf. Goursaud and others, 2019). This is supported by backward trajectories which have a clear west–east component crossing sea-ice-free areas in the Bellingshausen-Amundsen Sea (Supplementary Fig. S10). However, they also comprise easterly (Weddell Sea) and northerly directions (South America), since there is less cyclonic activity around Antarctica in summer (Lubin and others, 2008; Turner and others, 2019). The easterly component

is evidenced by the regional precipitation records, where EP station shows several maxima in February 2013 (Fig. 4e).

The distinct inverse relationship between  $\delta^{18}\text{O}$  and the SAM, as observed for the MMM-pattern, does not hold for the entire year 2013. The high  $\delta^{18}\text{O}$  values in January and February, for example, coincide with a strongly positive SAM ( $\text{MSI} > 2$ ; Marshall and others, 2006; Figs 9a, d). Instead, the d-excess behaves inversely to the SAM in this period. Overall, for both  $\delta^{18}\text{O}$  and the d-excess, the correlation with the SAM is negative but not statistically significant in 2013 ( $r = -0.3$ ,  $p = 0.4$  for  $\delta^{18}\text{O}$ ;  $r = -0.5$ ,  $p = 0.1$  for d-excess). To assess whether stable water isotopes in snow and firn from the northern AP can capture the subannual variability of the SAM, a longer core from the study area would be required.

We conclude that isotopic signals in firn cores from LCL and LP can be linked to specific synoptic situations occurring in the northern AP region with the MMM-pattern in winter 2013 as the most prominent example. This complements results of Hoffmann-Abdi and others (2021a), who showed that stable water isotopes in the snowpack on LCL recorded an atmospheric river-induced warm-air event prevailing in the northern AP region in March 2015. Due to the shortness of the dataset and the complexity of isotopic signal formation in snow and firn at the study site, it is difficult to conclude the transferability of identified relations with atmospheric circulation patterns to longer timescales.

## 5. Conclusions

High-accumulation areas such as the northern AP are challenging sites with respect to the interpretation of stable water isotope records from firn and ice cores. Here, we investigated possible connections between atmospheric conditions and the stable water isotope signals in six firn cores retrieved from two adjacent plateaus (LCL and LP) at the northernmost end of the AP between 2014 and 2016.

Firn-core  $\delta^{18}\text{O}$ -depth records show no clear seasonal cyclicity. Therefore, construction of reliable age models relies on the availability of glacio-chemical records with  $\text{H}_2\text{O}_2$  being the most suitable parameter for ALC. This method was used to derive an age model for core OH-9, independently of the already existing age scale for core OH-12 (Hoffmann-Abdi and others, 2021a). The two age models agree very well (offset:  $\sim 2$  weeks). Together, the cores cover the years 2012–2015, but we focused here on 2013, which is the overlapping period of all six firn cores.

Due to the very high snow accumulation (on average  $2500 \text{ kg m}^{-2} \text{ a}^{-1}$ ) on LCL and LP, the influence of post-depositional processes (e.g. diffusion) on the isotopic composition of snow and firn is reduced, leading to excellent signal preservation. Also, wind drift does not seem to have a notable impact on the stable water isotope composition of the snowpack, since isotopic signals are not only preserved within a single core, but also on a regional scale. The  $\delta^{18}\text{O}$  records of OH-9 and OH-12 show common patterns in the overlapping period, with a sequence of two remarkable minima enclosing a broad maximum (MMM-pattern) being the most striking one. The MMM-pattern spans the months of June through October 2013 and is found in all six firn cores. Therefore, it was used to place the cores on the same depth-age scale. Alignment of the cores remarkably improves cross-correlations not only between their stable water isotope records, but also their d-excess and density records. Signal-to-noise ratios are  $\sim 1.1$  for  $\delta^{18}\text{O}$  and  $\delta\text{D}$  and  $\sim 0.4$  for the d-excess with respect to the entire year 2013, and increase to about double when referring to the sub-annual scale.

Model-data intercomparison provides further evidence for the validity of constructed age models and hence the

representativeness of firn-core isotopic signals for specific synoptic situations in the region. The records of  $\delta^{18}\text{O}$  and d-excess of firn core OH-12 and those of the ECHAM6-wiso model show the same variability on annual and sub-annual scales (offset:  $\sim 1$  month), including the MMM-pattern. Statistically significant positive correlations between OH-12 and ECHAM6-wiso  $\delta^{18}\text{O}$  records for 2013 are limited to small areas on the western side of the AP and further south with values up to  $r \sim 0.7$  ( $p < 0.05$ ). For the d-excess, highest statistically significant positive correlations ( $r \sim 0.8$ ,  $p < 0.05$ ) are found in the Bellingshausen-Amundsen Sea, indicating predominantly westerly moisture transport pathways towards the study area. However, similar high correlations in the Weddell Sea and near the South American continent suggest that these regions are additional moisture sources for the northern AP.

For the investigated year 2013, the sub-annual variability of firn-core isotopic records has no equivalent in time series of near-surface air temperature either from reanalysis (ERA5) or from observations at the nearby OH, BH and EP stations. Instead, isotopic variability seems to be related to the variability of precipitation and moisture sources, for which temporal changes in the strength, position and zonality of the circumpolar westerlies are likely the main driver. The temporal variability of the westerly flow is in turn also reflected in temporal changes of the SAM. Results of backward trajectory modelling for the year 2013 reveal that  $\delta^{18}\text{O}$  minima are associated with long-range transport of maritime moisture towards the study area by predominantly (north-)westerly winds during positive SAM phases. In contrast,  $\delta^{18}\text{O}$  maxima are related to shorter moisture transport pathways with northerly (South America), southerly (Antarctic interior) or easterly (Weddell Sea) flow components during negative SAM phases. Especially, for the MMM-pattern in austral winter/spring 2013, the two  $\delta^{18}\text{O}$  minima are additionally associated with increased sea salt concentrations, indicating moisture origin and transport over open ocean areas. In contrast, the  $\delta^{18}\text{O}$  maximum corresponds to elevated values of black carbon and mineral dust, suggesting moisture advection from South America towards the study area.

Thus, we demonstrated that isotopic signals in firn cores from high-accumulation sites on the northern AP are representative of specific synoptic events in the region. The occurrence of such events is suggested to be related to atmospheric circulation changes and potentially linked to the (subannual) variability of the SAM. To assess the validity of this connection in detail, a longer isotope-geochemical record from the study area would be essential. The challenges associated with interpreting isotope-geochemical data from high-accumulation sites can be overcome by combining them with glacio-chemical data and atmospheric and isotopic modelling.

**Supplementary material.** The supplementary material for this article can be found at <https://doi.org/10.1017/jog.2023.79>

**Data availability.** The stable water isotope data of the six firn cores are available at <https://doi.pangaea.de/10.1594/PANGAEA.871083> (Fernandoy and others, 2017), <https://doi.org/10.1594/PANGAEA.939718> (Hoffmann-Abdi and others, 2021b) and <https://doi.pangaea.de/10.1594/PANGAEA.961100> (Hoffmann-Abdi and others, 2023a). The glacio-chemical data of firn cores OH-9 and OH-12 are available at <https://doi.org/10.1594/PANGAEA.939719> (Hoffmann-Abdi and others, 2021e) and <https://doi.pangaea.de/10.1594/PANGAEA.961101> (Hoffmann-Abdi and others, 2023b). Near-surface air temperatures and radiosonde measurements at Bellingshausen station are available at <https://www.scar.org/resources/ref-data-environmental-research/> (last access: 04.03.2022). Near-surface air temperature and precipitation records from Bernardo O'Higgins, Bellingshausen and Esperanza stations are available at <https://www.ncei.noaa.gov> (last access: 04.03.2022). ERA5 reanalysis data are available at <https://www.ecmwf.int/en/forecasts/dataset/ecmwf-reanalysis-v5> (last access: 09.02.2022). The KNMI Climate Explorer can be

accessed via <https://climexp.knmi.nl/> (last access: 20.02.2023). Monthly data on Antarctic sea ice extent are available at <https://nsidc.org/data/G02135/versions/3> (last access: 18.05.2022). Time series of the Marshall SAM Index are available at <https://climatedataguide.ucar.edu/climate-data/marshall-southern-annular-mode-sam-index-station-based> (last access: 26.05.2022). Time series of the ASL Actual Central Pressure Index Version 3, ASL longitudinal and latitudinal position are available at <https://climatedataguide.ucar.edu/climate-data/amundsen-sea-low-indices> (last access: 22.02.2023). Time series of latitude and strength of the Southern Hemisphere circumpolar westerly winds are available at <https://climatedataguide.ucar.edu/climate-data/southern-hemisphere-westerly-jet-strength-and-position> (last access: 29.09.2022). The HYSPLIT model can be accessed via <https://ready.arl.noaa.gov/HYSPLIT.php> (last access: 23.04.2022). The Global Data Assimilation System (GDAS) archives are available at <https://www.ready.noaa.gov/archives.php> (last access: 24.04.2022).

**Acknowledgments.** The presented work was partially funded by the FONDECYT project 11121551. Kirstin Hoffmann-Abdi was funded by an Elsa-Neumann Ph.D. scholarship awarded by the state of Berlin, Germany. We thank the Chilean government, i.e. the Instituto Antártico Chileno (INACH) and the Fuerza Aérea de Chile (FACH) for their support in the organization of field campaigns and for providing logistical facilities. We highly acknowledge the support of Delia Rodríguez Oroz and Dieter Tetzner in carrying out fieldwork and the support of the involved laboratory personnel at AWI, UNAB, BAS and DRI. We thank Sina Spors for her help with HYSPLIT backward trajectory modelling. We also thank two anonymous referees for their constructive comments that helped to substantially improve the manuscript.

**Author contributions.** Francisco Fernandoy designed the study and carried out the fieldwork, supported by Kirstin Hoffmann-Abdi and Hanno Meyer. Kirstin Hoffmann-Abdi and Hanno Meyer performed the stable water analyses of firn cores OH-7 and LP-01. Francisco Fernandoy carried out the density and stable water isotope measurements of firn core OH-11. High-resolution density profiles of firn cores OH-7 and LP-01 were generated by Kirstin Hoffmann-Abdi and Johannes Freitag. The glacio-chemical analyses of firn core OH-12 were performed by Kirstin Hoffmann-Abdi and Joseph R. McConnell. Elizabeth R. Thomas carried out the glacio-chemical analyses of firn core OH-9. Fyntan M. Shaw calculated diffusion lengths for all six firn cores. Martin Werner provided ECHAM6-wiso modelling results for the study area. Kirstin Hoffmann-Abdi performed HYSPLIT backward trajectory modelling for the study area. Kirstin Hoffmann-Abdi was responsible for data analysis, interpretation and writing of the manuscript, supported by Hanno Meyer and Christoph Schneider. All authors contributed to the data interpretation and the preparation of the final manuscript. All authors have read and agreed to the published version of the manuscript.

**Competing interest.** None.

## References

- Arndt S, Haas C, Meyer H, Peeken I and Krumpen T (2021) Recent observations of superimposed ice and snow ice on sea ice in the northwestern Weddell Sea. *The Cryosphere* **15**(9), 4165–4178. doi: [10.5194/tc-15-4165-2021](https://doi.org/10.5194/tc-15-4165-2021)
- Bagheri Dastgerdi S and 6 others (2021) Continuous monitoring of surface water vapour isotopic compositions at Neumayer Station III, East Antarctica. *The Cryosphere* **15**(10), 4745–4767. doi: [10.5194/tc-15-4745-2021](https://doi.org/10.5194/tc-15-4745-2021)
- Black RX and McDaniel BA (2007) Interannual variability in the southern hemisphere circulation organized by stratospheric final warming events. *Journal of the Atmospheric Sciences* **64**(8), 2968–2974. doi: [10.1175/JAS3979.1](https://doi.org/10.1175/JAS3979.1)
- Bond TC and 7 others (2007) Historical emissions of black and organic carbon aerosol from energy-related combustion, 1850–2000. *Global Biogeochemical Cycles* **21**(2), GB2018. doi: [10.1029/2006GB002840](https://doi.org/10.1029/2006GB002840)
- Bonne J-L and 7 others (2019) Resolving the controls of water vapour isotopes in the Atlantic sector. *Nature Communications* **10**(1), 1632. doi: [10.1038/s41467-019-09242-6](https://doi.org/10.1038/s41467-019-09242-6)
- Bracegirdle TJ (2018) Southern Hemisphere tropospheric westerly jet: 1979–present. *Polar Data Centre, Natural Environment Research Council, UK*. doi: [10.5285/3952a4fe-683a-42e7-a074-bdec41c8ab16](https://doi.org/10.5285/3952a4fe-683a-42e7-a074-bdec41c8ab16)
- Bracegirdle TJ, Hyder P and Holmes CR (2018) CMP5 diversity in southern westerly jet projections related to historical sea ice area: strong link to strengthening and weak link to shift. *Journal of Climate* **31**(1), 195–211. doi: [10.1175/jcli-d-17-0320.1](https://doi.org/10.1175/jcli-d-17-0320.1)



- Carrasco JF, Bozkurt D and Cordero RR** (2021) A review of the observed air temperature in the Antarctic Peninsula. Did the warming trend come back after the early 21st hiatus? *Polar Science* **28**, 100653. doi: [10.1016/j.polar.2021.100653](https://doi.org/10.1016/j.polar.2021.100653)
- Casado M and 6 others** (2021) Water isotopic signature of surface snow metamorphism in Antarctica. *Geophysical Research Letters* **48**(17), e2021GL093382. doi: [10.1029/2021GL093382](https://doi.org/10.1029/2021GL093382)
- Cauquoin A and Werner M** (2021) High-resolution nudged isotope modeling with ECHAM6-Wiso: impacts of updated model physics and ERA5 reanalysis data. *Journal of Advances in Modeling Earth Systems* **13**(11), e2021MS002532. doi: [10.1029/2021MS002532](https://doi.org/10.1029/2021MS002532)
- Cauquoin A, Werner M and Lohmann G** (2019) Water isotopes – climate relationships for the mid-Holocene and preindustrial period simulated with an isotope-enabled version of MPI-ESM. *Climate of the Past* **15**(6), 1913–1937. doi: [10.5194/cp-15-1913-2019](https://doi.org/10.5194/cp-15-1913-2019)
- Coplen TB and Wassenaar LI** (2015) LIMS for Lasers 2015 for achieving long-term accuracy and precision of  $\delta(2)\text{H}$ ,  $\delta(17)\text{O}$ , and  $\delta(18)\text{O}$  of waters using laser absorption spectrometry. *Rapid communications in mass spectrometry: RCM* **29**(22), 2122–2130. doi: [10.1002/rcm.7372](https://doi.org/10.1002/rcm.7372)
- Cordero RR and 20 others** (2022) Black carbon footprint of human presence in Antarctica. *Nature Communications* **13**(1), 984. doi: [10.1038/s41467-022-28560-w](https://doi.org/10.1038/s41467-022-28560-w)
- Dansgaard W** (1964) Stable isotopes in precipitation. *Tellus* **16**(4), 436–468. doi: [10.1111/j.2153-3490.1964.tb00181.x](https://doi.org/10.1111/j.2153-3490.1964.tb00181.x)
- Draxler RR and Hess G** (1998) An overview of the HYSPLIT\_4 modelling system for trajectories, dispersion, and deposition. *Australian Meteorological Magazine* **47**, 295–308.
- Fernandoy F, Meyer H and Tonelli M** (2012) Stable water isotopes of precipitation and firn cores from the northern Antarctic Peninsula region as a proxy for climate reconstruction. *The Cryosphere* **6**(2), 313–330. doi: [10.5194/tc-6-313-2012](https://doi.org/10.5194/tc-6-313-2012)
- Fernandoy F and 5 others** (2017) High resolution stable water isotope composition ( $\delta^{18}\text{O}$  and  $\text{dD}$ ) of two firn cores at the northern Antarctic Peninsula. *PANGAEA*. doi: [10.1594/PANGAEA.871083](https://doi.org/10.1594/PANGAEA.871083)
- Fernandoy F and 7 others** (2018) New insights into the use of stable water isotopes at the northern Antarctic Peninsula as a tool for regional climate studies. *The Cryosphere* **12**(3), 1069–1090. doi: [10.5194/tc-12-1069-2018](https://doi.org/10.5194/tc-12-1069-2018)
- Fiebig M, Lunder CR and Stohl A** (2009) Tracing biomass burning aerosol from South America to Troll Research Station, Antarctica. *Geophysical Research Letters* **36**(14), L14815. doi: [10.1029/2009GL038531](https://doi.org/10.1029/2009GL038531)
- Fisher DA, Reeh N and Clausen HB** (1985) Stratigraphic noise in time series derived from ice cores. *Annals of Glaciology* **7**, 76–83. doi: [10.3189/S0260305500005942](https://doi.org/10.3189/S0260305500005942)
- Fogt RL, Wovrosh AJ, Langen RA and Simmonds I** (2012) The characteristic variability and connection to the underlying synoptic activity of the Amundsen-Bellinghousen Seas Low. *Journal of Geophysical Research* **117**(D7), D07111. doi: [10.1029/2011JD017337](https://doi.org/10.1029/2011JD017337)
- Freitag J, Kipfstuhl S and Laepple T** (2013) Core-scale radioscopic imaging: a new method reveals density–calcium link in Antarctic firn. *Journal of Glaciology* **59**(218), 1009–1014. doi: [10.3189/2013JogG13J028](https://doi.org/10.3189/2013JogG13J028)
- Gabrielli P and 11 others** (2010) A major glacial-interglacial change in aeolian dust composition inferred from Rare Earth Elements in Antarctic ice. *Quaternary Science Reviews* **29**(1–2), 265–273. doi: [10.1016/j.quascirev.2009.09.002](https://doi.org/10.1016/j.quascirev.2009.09.002)
- Gaiero DM, Depetris PJ, Probst J-L, Bidart SM and Leleyter L** (2004) The signature of river- and wind-borne materials exported from Patagonia to the southern latitudes: a view from REEs and implications for paleoclimatic interpretations. *Earth and Planetary Science Letters* **219**(3–4), 357–376. doi: [10.1016/S0012-821X\(03\)00686-1](https://doi.org/10.1016/S0012-821X(03)00686-1)
- Goursaud S and 10 others** (2017) A 60-year ice-core record of regional climate from Adélie Land, coastal Antarctica. *The Cryosphere* **11**(1), 343–362. doi: [10.5194/tc-11-343-2017](https://doi.org/10.5194/tc-11-343-2017)
- Goursaud S and 6 others** (2019) Challenges associated with the climatic interpretation of water stable isotope records from a highly resolved firn core from Adélie Land, coastal Antarctica. *The Cryosphere* **13**(4), 1297–1324. doi: [10.5194/tc-13-1297-2019](https://doi.org/10.5194/tc-13-1297-2019)
- Grieman MM and 8 others** (2022) Continuous flow analysis methods for sodium, magnesium and calcium detection in the Skytrain ice core. *Journal of Glaciology* **68**(267), 90–100. doi: [10.1017/jog.2021.75](https://doi.org/10.1017/jog.2021.75)
- Gröning M, van Duren M and Andreescu L** (2007) Metrological characteristics of the conventional measurement scales for hydrogen and oxygen stable isotope amount ratios: The  $\delta$ -Scales. In Belli M, Fajgelj A and Sansone U (eds), *Combining and Reporting Analytical Results*. Cambridge: Royal Society of Chemistry, pp. 62–72. (Special Publications). doi: [10.1039/9781847557582-00062](https://doi.org/10.1039/9781847557582-00062)
- Haid V and Timmermann R** (2013) Simulated heat flux and sea ice production at coastal polynyas in the southwestern Weddell Sea. *Journal of Geophysical Research: Oceans* **118**(5), 2640–2652. doi: [10.1002/jgrc.20133](https://doi.org/10.1002/jgrc.20133)
- Herron MM and Langway CC** (1980) Firn densification: an empirical model. *Journal of Glaciology* **25**(93), 373–385. doi: [10.3189/S0022143000015239](https://doi.org/10.3189/S0022143000015239)
- Hersbach H and 42 others** (2020) The ERA5 global reanalysis. *Quarterly Journal of the Royal Meteorological Society* **146**(730), 1999–2049. doi: [10.1002/qj.3803](https://doi.org/10.1002/qj.3803)
- Hoffmann-Abdi K and 6 others** (2021a) Short-term meteorological and environmental signals recorded in a firn core from a high-accumulation site on Plateau Laclavere, Antarctic Peninsula. *Geosciences* **11**(10), 428. doi: [10.3390/geosciences11100428](https://doi.org/10.3390/geosciences11100428)
- Hoffmann-Abdi K and 6 others** (2021b) High-resolution stable water isotope composition of firn core OH-12 from Plateau Laclavere, northern Antarctic Peninsula. *PANGAEA*. doi: [10.1594/PANGAEA.939718](https://doi.org/10.1594/PANGAEA.939718)
- Hoffmann-Abdi K and 6 others** (2021c) High-resolution black carbon data of firn core OH-12 from Plateau Laclavere, northern Antarctic Peninsula. *PANGAEA*. doi: [10.1594/PANGAEA.939714](https://doi.org/10.1594/PANGAEA.939714)
- Hoffmann-Abdi K and 6 others** (2021d) High-resolution non-sea-salt sulphur and sea-salt sodium data of firn core OH-12 from Plateau Laclavere, northern Antarctic Peninsula. *PANGAEA*. doi: [10.1594/PANGAEA.939716](https://doi.org/10.1594/PANGAEA.939716)
- Hoffmann-Abdi K and 6 others** (2021e) High-resolution stable water isotope and glacio-chemical composition of a firn core from the northern Antarctic Peninsula. *PANGAEA*. doi: [10.1594/PANGAEA.939719](https://doi.org/10.1594/PANGAEA.939719)
- Hoffmann-Abdi K and 9 others** (2023a) High-resolution stable water isotope composition of firn cores OH-7, OH-11 and LP-01 from the northern Antarctic Peninsula. *PANGAEA*. doi: [10.1594/PANGAEA.961100](https://doi.org/10.1594/PANGAEA.961100)
- Hoffmann-Abdi K and 8 others** (2023b) High-resolution glacio-chemical composition of firn cores OH-9 and OH-12 from the northern Antarctic Peninsula. *PANGAEA*. doi: [10.1594/PANGAEA.961101](https://doi.org/10.1594/PANGAEA.961101)
- Hosking JS, Orr A, Marshall GJ, Turner J and Phillips T** (2013) The influence of the Amundsen–Bellingshausen seas low on the climate of West Antarctica and its representation in coupled climate model simulations. *Journal of Climate* **26**(17), 6633–6648. doi: [10.1175/JCLI-D-12-00813.1](https://doi.org/10.1175/JCLI-D-12-00813.1)
- Hosking JS, Orr A, Bracegirdle TJ and Turner J** (2016) Future circulation changes off West Antarctica: sensitivity of the Amundsen Sea Low to projected anthropogenic forcing. *Geophysical Research Letters* **43**(1), 367–376. doi: [10.1002/2015GL067143](https://doi.org/10.1002/2015GL067143)
- Hughes AG and 6 others** (2021) The role of sublimation as a driver of climate signals in the water isotope content of surface snow: laboratory and field experimental results. *The Cryosphere* **15**(10), 4949–4974. doi: [10.5194/tc-15-4949-2021](https://doi.org/10.5194/tc-15-4949-2021)
- Jumelet J and 7 others** (2020) Detection of aerosols in Antarctica from long-range transport of the 2009 Australian Wildfires. *Journal of Geophysical Research: Atmospheres* **125**(23), e2020JD032542. doi: [10.1029/2020JD032542](https://doi.org/10.1029/2020JD032542)
- Kaspari S and 6 others** (2004) Climate variability in West Antarctica derived from annual accumulation-rate records from ITASE firn/ice cores. *Annals of Glaciology* **39**, 585–594. doi: [10.3189/172756404781814447](https://doi.org/10.3189/172756404781814447)
- Kaspari S, Dixon DA, Sneed SB and Handley MJ** (2005) Sources and transport pathways of marine aerosol species into West Antarctica. *Annals of Glaciology* **41**, 1–9. doi: [10.3189/172756405781813221](https://doi.org/10.3189/172756405781813221)
- Kreutz KJ and 5 others** (2000) Sea level pressure variability in the Amundsen Sea region inferred from a West Antarctic glaciochemical record. *Journal of Geophysical Research* **105**(D3), 4047–4059. doi: [10.1029/1999JD901069](https://doi.org/10.1029/1999JD901069)
- Laepple T and 5 others** (2018) On the similarity and apparent cycles of isotopic variations in East Antarctic snow pits. *The Cryosphere* **12**(1), 169–187. doi: [10.5194/tc-12-169-2018](https://doi.org/10.5194/tc-12-169-2018)
- Lee DY, Petersen MR and Lin W** (2019) The southern annular mode and southern ocean surface westerly winds in E3SM. *Earth and Space Science* **6**(12), 2624–2643. doi: [10.1029/2019EA000663](https://doi.org/10.1029/2019EA000663)
- Limpasuvan V and Hartmann DL** (2000) Wave-maintained annular modes of climate variability\*. *Journal of Climate* **13**(24), 4414–4429. doi: [10.1175/1520-0442\(2000\)013<4414:WMAMOC>2.0.CO;2](https://doi.org/10.1175/1520-0442(2000)013<4414:WMAMOC>2.0.CO;2)
- Liu P and 12 others** (2021) Improved estimates of preindustrial biomass burning reduce the magnitude of aerosol climate forcing in the Southern Hemisphere. *Science Advances* **7**(22), eabc1379. doi: [10.1126/sciadv.abc1379](https://doi.org/10.1126/sciadv.abc1379)
- Lubin D, Wittenmyer RA, Bromwich DH and Marshall GJ** (2008) Antarctic Peninsula mesoscale cyclone variability and climatic impacts influenced by

- the SAM. *Geophysical Research Letters* **35**(2), L02808. doi: [10.1029/2007GL032170](https://doi.org/10.1029/2007GL032170)
- Maclennan ML, Lenaerts JTM, Shields C and Wille JD** (2022) Contribution of atmospheric rivers to Antarctic precipitation. *Geophysical Research Letters* **49**(18), e2022GL100585. doi: [10.1029/2022GL100585](https://doi.org/10.1029/2022GL100585)
- Marshall GJ** (2003) Trends in the southern annular mode from observations and reanalyses. *Journal of Climate* **16**(24), 4134–4143. doi: [10.1175/1520-0442\(2003\)016<4134:TTSAM>2.0.CO;2](https://doi.org/10.1175/1520-0442(2003)016<4134:TTSAM>2.0.CO;2)
- Marshall GJ and Thompson DWJ** (2016) The signatures of large-scale patterns of atmospheric variability in Antarctic surface temperatures. *Journal of Geophysical Research: Atmospheres* **121**(7), 3276–3289. doi: [10.1002/2015JD024665](https://doi.org/10.1002/2015JD024665)
- Marshall GJ, Orr A, van Lipzig NPM and King JC** (2006) The impact of a changing southern hemisphere annular mode on Antarctic peninsula summer temperatures. *Journal of Climate* **19**(20), 5388–5404. doi: [10.1175/JCLI3844.1](https://doi.org/10.1175/JCLI3844.1)
- Marshall GJ, Thompson DWJ and van den Broeke MR** (2017) The signature of southern hemisphere atmospheric circulation patterns in Antarctic precipitation. *Geophysical Research Letters* **44**(22), 11580–11589. doi: [10.1002/2017GL075998](https://doi.org/10.1002/2017GL075998)
- Masson-Delmotte V and 6 others** (2003) Recent southern Indian Ocean climate variability inferred from a Law Dome ice core: new insights for the interpretation of coastal Antarctic isotopic records. *Climate Dynamics* **21**(2), 153–166. doi: [10.1007/s00382-003-0321-9](https://doi.org/10.1007/s00382-003-0321-9)
- Masson-Delmotte V and 35 others** (2008) A review of Antarctic surface snow isotopic composition: observations, atmospheric circulation, and isotopic modeling\*. *Journal of Climate* **21**(13), 3359–3387. doi: [10.1175/2007JCLI2139.1](https://doi.org/10.1175/2007JCLI2139.1)
- McConnell JR, Lamorey GW, Lambert SW and Taylor KC** (2002) Continuous ice-core chemical analyses using inductively coupled plasma mass spectrometry. *Environmental Science & Technology* **36**(1), 7–11. doi: [10.1021/es011088z](https://doi.org/10.1021/es011088z)
- McConnell JR and 9 others** (2007) 20th-Century industrial black carbon emissions altered Arctic climate forcing. *Science* **317**(5843), 1381–1384. doi: [10.1126/science.1144856](https://doi.org/10.1126/science.1144856)
- Mchedlishvili A, Spreen G, Melsheimer C and Huntemann M** (2022) Weddell Sea polynya analysis using SMOS-SMAP apparent sea ice thickness retrieval. *The Cryosphere* **16**(2), 471–487. doi: [10.5194/tc-16-471-2022](https://doi.org/10.5194/tc-16-471-2022)
- Merlivat L and Jouzel J** (1979) Global climatic interpretation of the deuterium-oxygen 18 relationship for precipitation. *Journal of Geophysical Research* **84**(C8), 5029–5033. doi: [10.1029/JC084iC08p05029](https://doi.org/10.1029/JC084iC08p05029)
- Moran T, Marshall SJ and Sharp MJ** (2011) Isotope thermometry in melt-affected ice cores. *Journal of Geophysical Research* **116**(F2), F02010. doi: [10.1029/2010JF001738](https://doi.org/10.1029/2010JF001738)
- Münch T and Laepple T** (2018) What climate signal is contained in decadal-to centennial-scale isotope variations from Antarctic ice cores? *Climate of the Past* **14**(12), 2053–2070. doi: [10.5194/cp-14-2053-2018](https://doi.org/10.5194/cp-14-2053-2018)
- Münch T, Kipfstuhl S, Freitag J, Meyer H and Laepple T** (2016) Regional climate signal vs. local noise: a two-dimensional view of water isotopes in Antarctic firn at Kohnen Station, Dronning Maud Land. *Climate of the Past* **12**(7), 1565–1581. doi: [10.5194/cp-12-1565-2016](https://doi.org/10.5194/cp-12-1565-2016)
- Münch T, Kipfstuhl S, Freitag J, Meyer H and Laepple T** (2017) Constraints on post-depositional isotope modifications in East Antarctic firn from analysing temporal changes of isotope profiles. *The Cryosphere* **11**(5), 2175–2188. doi: [10.5194/tc-11-2175-2017](https://doi.org/10.5194/tc-11-2175-2017)
- Neumann TA and Waddington ED** (2004) Effects of firn ventilation on isotopic exchange. *Journal of Glaciology* **50**(169), 183–194. doi: [10.3189/172756504781830150](https://doi.org/10.3189/172756504781830150)
- Orr A and 6 others** (2004) A 'low-level' explanation for the recent large warming trend over the western Antarctic Peninsula involving blocked winds and changes in zonal circulation. *Geophysical Research Letters* **31**(6), L06204. doi: [10.1029/2003GL019160](https://doi.org/10.1029/2003GL019160)
- Pereira EB, Evangelista H, Pereira KCD, Cavalcanti IFA and Setzer AW** (2006) Apportionment of black carbon in the South Shetland Islands, Antarctic Peninsula. *Journal of Geophysical Research* **111**(D3), D03303. doi: [10.1029/2005JD006086](https://doi.org/10.1029/2005JD006086)
- Perren BB and 6 others** (2020) Southward migration of the Southern Hemisphere westerly winds corresponds with warming climate over centennial timescales. *Communications Earth & Environment* **1**(1), 58. doi: [10.1038/s43247-020-00059-6](https://doi.org/10.1038/s43247-020-00059-6)
- Pfahl S and Sodemann H** (2014) What controls deuterium excess in global precipitation? *Climate of the Past* **10**(2), 771–781. doi: [10.5194/cp-10-771-2014](https://doi.org/10.5194/cp-10-771-2014)
- Raphael MN and 8 others** (2016) The Amundsen sea low: variability, change, and impact on Antarctic climate. *Bulletin of the American Meteorological Society* **97**(1), 111–121. doi: [10.1175/BAMS-D-14-00018.1](https://doi.org/10.1175/BAMS-D-14-00018.1)
- Ritter F and 9 others** (2016) Isotopic exchange on the diurnal scale between near-surface snow and lower atmospheric water vapor at Kohnen station, East Antarctica. *The Cryosphere* **10**(4), 1647–1663. doi: [10.5194/tc-10-1647-2016](https://doi.org/10.5194/tc-10-1647-2016)
- Rolph G, Stein A and Stunder B** (2017) Real-time environmental applications and display system: READY. *Environmental Modelling & Software* **95**, 210–228. doi: [10.1016/j.envsoft.2017.06.025](https://doi.org/10.1016/j.envsoft.2017.06.025)
- Röthlisberger R and 6 others** (2000) Technique for continuous high-resolution analysis of trace substances in firn and ice cores. *Environmental Science & Technology* **34**(2), 338–342. doi: [10.1021/es9907055](https://doi.org/10.1021/es9907055)
- Rozanski K, Araguás-Araguás L and Gonfiantini R** (1993) Isotopic patterns in modern global precipitation. In Swart PK, Lohmann KC, Mckenzie J and Savin S (eds), *Climate Change in Continental Isotopic Records*. Washington, DC: American Geophysical Union, pp. 1–36. (Geophysical Monograph Series). doi: [10.1029/GM078p0001](https://doi.org/10.1029/GM078p0001)
- Schmidt GA, LeGrande AN and Hoffmann G** (2007) Water isotope expressions of intrinsic and forced variability in a coupled ocean-atmosphere model. *Journal of Geophysical Research* **112**(D10), D10103. doi: [10.1029/2006JD007781](https://doi.org/10.1029/2006JD007781)
- Severinghaus JP and 12 others** (2010) Deep air convection in the firn at a zero-accumulation site, central Antarctica. *Earth and Planetary Science Letters* **293**(3–4), 359–367. doi: [10.1016/j.epsl.2010.03.003](https://doi.org/10.1016/j.epsl.2010.03.003)
- Sheshadri A, Plumb RA and Domeisen DIV** (2014) Can the delay in Antarctic polar vortex breakup explain recent trends in surface westerlies? *Journal of the Atmospheric Sciences* **71**(2), 566–573. doi: [10.1175/JAS-D-12-0343.1](https://doi.org/10.1175/JAS-D-12-0343.1)
- Sinclair KE, Bertler NAN and Trompeter WJ** (2010) Synoptic controls on precipitation pathways and snow delivery to high-accumulation ice core sites in the Ross Sea region, Antarctica. *Journal of Geophysical Research* **115**(D22), D22112. doi: [10.1029/2010JD014383](https://doi.org/10.1029/2010JD014383)
- Steen-Larsen HC and 23 others** (2011) Understanding the climatic signal in the water stable isotope records from the NEEM shallow firn/ice cores in northwest Greenland. *Journal of Geophysical Research* **116**(D6), D06108. doi: [10.1029/2010JD014311](https://doi.org/10.1029/2010JD014311)
- Steig EJ and 16 others** (2005) High-resolution ice cores from US ITASE (West Antarctica): development and validation of chronologies and determination of precision and accuracy. *Annals of Glaciology* **41**, 77–84. doi: [10.3189/172756405781813311](https://doi.org/10.3189/172756405781813311)
- Stein AF and 5 others** (2015) NOAA's HYSPLIT atmospheric transport and dispersion modeling system. *Bulletin of the American Meteorological Society* **96**(12), 2059–2077. doi: [10.1175/BAMS-D-14-00110.1](https://doi.org/10.1175/BAMS-D-14-00110.1)
- Stenni B and 14 others** (2010) The deuterium excess records of EPICA Dome C and Dronning Maud Land ice cores (East Antarctica). *Quaternary Science Reviews* **29**(1–2), 146–159. doi: [10.1016/j.quascirev.2009.10.009](https://doi.org/10.1016/j.quascirev.2009.10.009)
- Stevens B and 17 others** (2013) Atmospheric component of the MPI-M Earth System Model: ECHAM6. *Journal of Advances in Modeling Earth Systems* **5**(2), 146–172. doi: [10.1002/jame.20015](https://doi.org/10.1002/jame.20015)
- Thomas ER and Tetzner DR** (2019) The climate of the Antarctic Peninsula during the twentieth century: evidence from ice cores. In Kanao M, Toyokuni G and Yamamoto M (eds), *Antarctica - A Key To Global Change*. London, UK: IntechOpen. doi: [10.5772/intechopen.75265](https://doi.org/10.5772/intechopen.75265)
- Thompson DWJ and Wallace JM** (2000) Annular modes in the extratropical circulation. Part I: month-to-month variability\*. *Journal of Climate* **13**(5), 1000–1016. doi: [10.1175/1520-0442\(2000\)013<1000:AMITEC>2.0.CO;2](https://doi.org/10.1175/1520-0442(2000)013<1000:AMITEC>2.0.CO;2)
- Thompson DWJ and Solomon S** (2002) Interpretation of recent Southern Hemisphere climate change. *Science* **296**(5569), 895–899. doi: [10.1126/science.1069270](https://doi.org/10.1126/science.1069270)
- Thompson DWJ, Baldwin MP and Solomon S** (2005) Stratosphere-troposphere coupling in the southern hemisphere. *Journal of the Atmospheric Sciences* **62**(3), 708–715. doi: [10.1175/JAS-3321.1](https://doi.org/10.1175/JAS-3321.1)
- Town MS, Warren SG, Walden VP and Waddington ED** (2008) Effect of atmospheric water vapor on modification of stable isotopes in near-surface snow on ice sheets. *Journal of Geophysical Research* **113**(D24), D24303. doi: [10.1029/2008JD009852](https://doi.org/10.1029/2008JD009852)
- Turner J, Phillips T, Hosking JS, Marshall GJ and Orr A** (2013) The Amundsen Sea low. *International Journal of Climatology* **33**(7), 1818–1829. doi: [10.1002/joc.3558](https://doi.org/10.1002/joc.3558)
- Turner J and 12 others** (2019) The dominant role of extreme precipitation events in Antarctic snowfall variability. *Geophysical Research Letters* **46**(6), 3502–3511. doi: [10.1029/2018GL081517](https://doi.org/10.1029/2018GL081517)
- Uemura R, Matsui Y, YOSHIMURA K, Motoyama H and Yoshida N** (2008) Evidence of deuterium excess in water vapor as an indicator of ocean surface conditions. *Journal of Geophysical Research*, **113**(D19), D19114. doi: [10.1029/2008JD010209](https://doi.org/10.1029/2008JD010209)

- van Geldern R and Barth JA** (2012) Optimization of instrument setup and post-run corrections for oxygen and hydrogen stable isotope measurements of water by isotope ratio infrared spectroscopy (IRIS). *Limnology and Oceanography: Methods* **10**(12), 1024–1036. doi: [10.4319/lom.2012.10.1024](https://doi.org/10.4319/lom.2012.10.1024)
- Vaughan DG and 8 others** (2003) Recent rapid regional climate warming on the Antarctic Peninsula. *Climatic Change* **60**(3), 243–274. doi: [10.1023/A:1026021217991](https://doi.org/10.1023/A:1026021217991)
- Wahl S and 7 others** (2022) Atmosphere-snow exchange explains surface snow isotope variability. *Geophysical Research Letters* **49**(20), e2022GL099529. doi: [10.1029/2022GL099529](https://doi.org/10.1029/2022GL099529)
- Wegner A and 9 others** (2012) Change in dust variability in the Atlantic sector of Antarctica at the end of the last deglaciation. *Climate of the Past* **8**(1), 135–147. doi: [10.5194/cp-8-135-2012](https://doi.org/10.5194/cp-8-135-2012)
- Wille JD and 6 others** (2019) West Antarctic surface melt triggered by atmospheric rivers. *Nature Geoscience* **12**(11), 911–916. doi: [10.1038/s41561-019-0460-1](https://doi.org/10.1038/s41561-019-0460-1)
- Wille JD and 14 others** (2022) Intense atmospheric rivers can weaken ice shelf stability at the Antarctic Peninsula. *Communications Earth & Environment* **3**(1), 90. doi: [10.1038/s43247-022-00422-9](https://doi.org/10.1038/s43247-022-00422-9)
- Wolff EW and Cachier H** (1998) Concentrations and seasonal cycle of black carbon in aerosol at a coastal Antarctic station. *Journal of Geophysical Research: Atmospheres* **103**(D9), 11033–11041. doi: [10.1029/97JD01363](https://doi.org/10.1029/97JD01363)